

Differentiable Artificial Reverberation

Sungho Lee, Hyeong-Seok Choi, and Kyogu Lee

Abstract—We propose differentiable artificial reverberation (DAR), a family of artificial reverberation (AR) models implemented in a deep learning framework. Combined with the modern deep neural networks (DNNs), the differentiable structure of DAR allows training loss gradients to be back-propagated in an end-to-end manner. Most of the AR models bottleneck training speed when implemented “as is” in the time domain and executed with a parallel processor like GPU due to their infinite impulse response (IIR) filter components. We tackle this by further developing a recently proposed acceleration technique, which borrows the frequency-sampling method (FSM). With the proposed DAR models, we aim to solve an artificial reverberation parameter (ARP) estimation task in a unified approach. We design an ARP estimation network applicable to both analysis-synthesis (RIR-to-ARP) and blind estimation (reverberant-speech-to-ARP) tasks. And using different DAR models only requires slightly a different decoder configuration. This way, the proposed DAR framework overcomes the previous methods’ limitations of task-dependency and AR-model-dependency.

Index Terms—Digital Signal Processing, Acoustics, Reverberation, Artificial Reverberation, Deep Learning.

I. INTRODUCTION

Reverberation is ubiquitous in a real acoustic environment. It provides the listeners psychoacoustic cues for spatial presence, and thus adding appropriate reverberation to dry audio is crucial for plausible listening [1]–[3]. *Artificial reverberation* (AR), digital filters that mimic real-world reverberation, have been developed to achieve such auditory effects [4]–[6]. Most AR models aim for computational efficiency with sparse and highly parameterized filters. Still, the auditory effects produced by them are perceptually similar to real-world reverberation. In this regard, AR models have various applications such as virtual auditory scene generation [7], [8], room acoustic enhancement [9], post-production and recording [10], and many more.

To leverage the power of deep learning for AR, we introduce *differentiable artificial reverberation* (DAR), a family of AR models implemented in a deep learning framework. Especially, we propose differentiable Filtered Velvet Noise (FVN) [11], advanced FVN (ADV-FVN), and Feedback Delay Network (FDN) [12]. These models enable gradient propagation and end-to-end training of a deep neural network (DNN).

It is well-known that any linear time-invariant (LTI) filter (e.g., AR model) is differentiable; loss gradients with respect to its parameters can be computed [13]–[16]. However, most AR models are composed of infinite impulse response (IIR) filters whose recurrent computation bottleneck the speed of forward-pass (i.e., filtering) and backpropagation in a parallel processor like GPU. To tackle this, we borrow the *frequency-sampling method* (FSM) [17] to get a finite impulse response (FIR)

Manuscript in progress. The authors are with the Music and Audio Research Group (MARG), Seoul National University, Seoul, Republic of Korea (e-mail: sh-lee@snu.ac.kr; kekepa15@snu.ac.kr; kglee@snu.ac.kr).

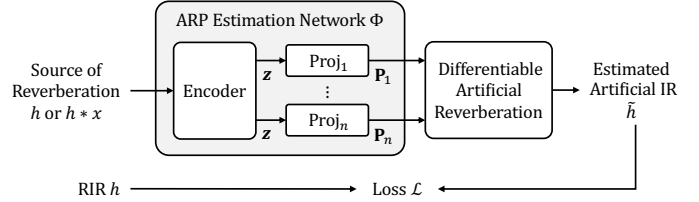


Fig. 1. Proposed ARP estimation framework. With DAR models, loss gradients $\partial\mathcal{L}/\partial\mathbf{P}_1, \dots, \partial\mathcal{L}/\partial\mathbf{P}_n$ can be back-propagated through the DAR models. Then, the ARP estimation network Φ can be trained end-to-end. The network can simultaneously perform the analysis-synthesis (RIR h input) and blind estimation (reverberant speech $h * x$ input). Using a different DAR model only requires changing the ARP-groupwise projection layers $\text{Proj}_1, \dots, \text{Proj}_n$, being closer to an AR-model-independent framework.

approximation of each IIR filter without any recurrent step. With the FIRs, filtering (i.e., convolution) can be performed efficiently in the frequency domain with a Fast Fourier Transform (FFT). While the FSM was initially proposed as an FIR design method, exploiting it for the DNN training acceleration was first appeared in [18]. To apply such a technique to the AR models, we first conduct theoretical analysis on the reliability of the FSM. Then, we derive differentiable IIR filters, which have parameters that can be easily optimized and will be used as building blocks of the DAR models.

We demonstrate the advantages of the differentiable structure of DAR with artificial reverberation parameter (ARP) estimation task, i.e., finding ARPs that match target reverberation¹. When the target is given as a room impulse response (room IR, RIR) h , it becomes the *analysis-synthesis* task. If the target is indirectly provided with reverberant speech $h * x$ where x is dry speech, it becomes the *blind estimation* task. Most previous methods [10], [11], [19]–[22] are limited to a specific AR model (AR-model-dependent) and proposed for one of the two tasks, but not both (task-dependent). We overcome these shortcomings with the DAR models. As shown in Figure 1, we connect an *ARP estimation network* and the DAR model so that the training is done end-to-end. The network takes raw audio as input, either h or $h * x$. This way, the network can perform the two tasks as if they are the same. Also, we factorize the network into an AR-model-invariant encoder and ARP-groupwise projection layers so that using a different DAR model requires changing only the latter.

We summarize our contributions as follows:

- We analyze and develop the FSM for the differentiable IIR filters from a general perspective.
- Using the differentiable IIR filters as building blocks, we derive differentiable FVN, ADV-FVN, and FDN.
- We propose an ARP estimation network architecture that is independent of the DAR model or task.

¹Audio samples are available at <https://sh-lee97.github.io/DAR-samples/>.

The rest of the paper is organized as follows: we first review related works in Section II. We develop the FSM in Section III and build the DAR models in Section IV. The ARP estimation tasks and our network are explained in Section V. Experimental setup and its evaluation results are reported in Section VI and VII, respectively. We conclude the paper in Section VIII, with proofs of the FSM-related equations in Appendix A.

II. RELATED WORKS

A. Differentiable Digital Signal Processing

Traditional digital signal processing (DSP) and deep learning are closely related. [23] modeled compressor with a temporal convolutional network, which is an extension of a classical Wiener-Hammerstein model [24]. Direct import of DSP components to the deep-learning frameworks recently gained interest since they provide interpretable representations with explicit inductive biases of DSP knowledge. [25] built a differentiable harmonic-plus-noise model [26] with such components and trained its parameter estimator for sound synthesis. In the case of LTI filters, direct counterparts of an FIR and IIR filter exist in the deep-learning literature: a convolutional and recurrent layer, respectively [16]. Since IIR filter bottlenecks the training speed, [18] borrowed the FSM (or so-called `freqz` method) [17] and trained a parametric equalizer's (PEQ's) parameter estimator. [27] stacked the differentiable PEQs and nonlinearities (again, it is a cascaded Wiener-Hammerstein model) to mimic an analog distortion pedal. Upon these works, we clarify the reliability of the FSM, provide a general differentiable LTI filter based on a state-variable filter (SVF) parameterization [28], [29], and build the DAR models with it.

B. ARP Estimation

1) *Analysis-synthesis*: [19] addressed an analysis-synthesis task with proposed energy decay relief (EDR) representation of an RIR. [20] found FDN parameters using a genetic algorithm equipped with IIR filter optimization subroutines. [11] proposed FVN, ADV-FVN, and algorithms that fit these models to given late reverberation. All these methods are specialized and limited to specific AR models.

Instead, [21] trained a DNN for the analysis-synthesis task of FDN. This reduces the engineering burden by replacing the AR-model-dependent estimation methods with more general deep learning approaches. However, direct supervision on the ARPs requires generating training data (i.e., RIR-ARP pairs) for every different FDN configuration. Furthermore, ARP estimation is a one-to-many task; different ARPs could yield the same IR, which complicates the ground-truth data preparation and the training process. We overcome this issue with the end-to-end pipeline achieved with DAR; a loss between the target IR and the estimation is calculated in the raw audio domain, and the loss gradient is propagated without any explicit ARP evaluation.

2) *Blind Estimation*: [22] addressed a preset recommendation (i.e., classification) of an AR plugin from a given reference $h * x$ in a supervised way. [10] generated reverberant-speech-and-AR-plugin-parameter pairs and trained a DNN with it. Both works suffer the same shortcoming of [21]. Also, they are only applicable to a small set of the AR plugin presets or parameters

that control the actual ARPs. Our method directly estimates the ARPs. Instead of the direct ARP estimation, a two-stage approach with a reverberation parameter (RP) estimation (e.g., reverberation time T_{30} estimation) task [30]–[33] followed by an RP-to-ARP task [34]–[36] could be a possible alternative. However, unlike the ARPs, perceptually different reverberations can be mapped to the same RP, which causes information loss.

III. FREQUENCY-SAMPLING METHOD FOR DIFFERENTIABLE IIR FILTERS

For any real LTI filter H^2 , its frequency response $H(e^{j\omega})$ is continuous, 2π -periodic, and conjugate symmetric. To obtain an approximation of H , we *frequency-sample* $H(e^{j\omega})$ at angular frequencies $\omega_k = 2\pi k/N$ where $k = 0, \dots, \lfloor N/2 \rfloor$ [17]. We denote the frequency-sampled filter with subscript N , i.e., H_N .

$$H_N[k] = H(e^{j\omega_k}). \quad (1)$$

Note that the frequency-sampling can also be defined on transfer functions $H(z)$ with $z = e^{j\omega_k}$.

Since each sampling is independent, H_N can be generated simultaneously with a parallel processor like GPU. Furthermore, the order of frequency-sampling $(\cdot)_N$ and other basic arithmetic operations does not matter. Therefore, we can frequency-sample an IIR filter $H(z) = (\sum_{m=0}^M \beta_m z^{-m}) / (\sum_{m=0}^M \alpha_m z^{-m})$ by combining frequency-sampled m -sample delays $(z^{-m})_N$.

$$H_N[k] = \left(\frac{\sum_{m=0}^M \beta_m z^{-m}}{\sum_{m=0}^M \alpha_m z^{-m}} \right)_N [k] = \frac{\sum_{m=0}^M \beta_m (z^{-m})_N [k]}{\sum_{m=0}^M \alpha_m (z^{-m})_N [k]}. \quad (2)$$

Since $(z^{-m})_N [k] = e^{-j2\pi km/N}$, using the widely-used deep-learning frameworks, we generate $(z^{-m})_N \in \mathbb{C}^{\lfloor N/2 \rfloor + 1}$ as a single tensor z_m by

$$\text{angle} = 2 * \text{pi} * \text{arange}(N // 2 + 1) / N, \quad (3a)$$

$$z_m = \text{e}^{**}(-1j * \text{angle} * m). \quad (3b)$$

Then, we apply equation (2) to z_0, \dots, z_M with basic tensor operations and obtain every sample of H_N in parallel. A time-domain representation of H_N is a length- N FIR $h_N[n]$, inverse discrete Fourier transform (inverse DFT) of $H_N[k]$, i.e.,

$$h_N[n] = \frac{1}{N} \sum_{k=0}^{N-1} H_N[k] e^{j\omega_k n} (u[n] - u[n - N]) \quad (4)$$

where $u[n]$ is a unit step function.

A. Reliability of the Frequency-Sampling Method

An n^{th} Fourier coefficient of a stable LTI filter's frequency response $H(e^{j\omega})$ is $h[-n]$. Therefore, any FIR filter's frequency response is band-limited. The opposite case holds for an IIR filter, and inevitable information loss caused by the frequency-sampling appears as *time-aliasing* [37].

$$h_N[n] = \sum_{m=0}^{\infty} h[mN + n] (u[n] - u[n - N]). \quad (5)$$

²We prioritize the conventional DSP notations. We denote an LTI filter with an upper-case letter, e.g., H . $H(z)$, $H(e^{j\omega})$, and $h[n]$ (or simply h) denote its transfer function, frequency response, and IR, respectively. z , ω , and n are preserved to represent the z -domain variable, the discrete-time Fourier transform (DTFT) domain frequency, and the discrete-time index, respectively.

Now assume that H has M distinct poles $\nu_i \in \mathbb{C}$, each with a multiplicity $r_i \in \mathbb{N}$. When N increases, the time-aliasing error of H_N in the l_2 distance³ $\|H - H_N\|_2 := \|h[n] - h_N[n]\|_2 = \|H(e^{j\omega}) - H_N(e^{j\omega})\|_2 / \sqrt{2\pi}$ asymptotically decreases as

$$\|H - H_N\|_2 = \sum_{i=1}^M O(N^{r_i-1} |\nu_i|^N). \quad (6)$$

Therefore, H_N becomes a reliable representation of H when the sampling resolution N is sufficiently high. However, higher N requires more memory and computation; thus, compensation must be made. Refer to Figure 2 for the illustration.

FSM also changes loss gradients. If an LTI filter \hat{H} has a well-defined parameter p (derivatives of pole/zeros with respect to p exist and are finite), deviation of a squared l_2 loss gradient with respect to p asymptotically decreases as

$$\left| \frac{\partial}{\partial p} \|H - \hat{H}\|_2^2 - \frac{\partial}{\partial p} \|H - \hat{H}_N\|_2^2 \right| = \sum_{i=1}^M O(N^{3r_i-1} |\nu_i|^N). \quad (7)$$

For proofs of the equations, refer to Appendix A.

Note that the FSM is a suboptimal FIR design method [37]. Nevertheless, to the authors' best knowledge, it is the fastest non-iterative method. Also, the FIR length N only matters for the reliability of the filter's estimator since the original filter will be used after the training.

B. Differentiable Dense IIR Filter with State-variable Filters

Since arbitrary IIR filter can be expressed as serially cascaded biquads (second-order IIR filters), we can obtain a differentiable IIR filter \tilde{H} as a product of frequency-sampled biquads⁴ $(H_i)_N$.

$$\tilde{H}[k] = H_N[k] = \prod_i (H_i)_N[k]. \quad (8)$$

Furthermore, each biquad H_i can be expressed with a linear combination of *state variable filter* (SVF) outputs, i.e., lowpass H_i^{LP} , bandpass H_i^{BP} , and highpass H_i^{HP} with their mixing gains m_i^{LP} , m_i^{BP} , and m_i^{HP} [29], [38].

$$H_i(z) = \frac{\beta_{i,0} + \beta_{i,1}z^{-1} + \beta_{i,2}z^{-2}}{\alpha_{i,0} + \alpha_{i,1}z^{-1} + \alpha_{i,2}z^{-2}} \quad (9a)$$

$$= m_i^{\text{LP}} H_i^{\text{LP}}(z) + m_i^{\text{BP}} H_i^{\text{BP}}(z) + m_i^{\text{HP}} H_i^{\text{HP}}(z). \quad (9b)$$

H_i^{LP} , H_i^{BP} , and H_i^{HP} share a common cutoff $f_i = \tan(\pi\omega_i/\omega_s)$ where ω_s is the sampling rate and ω_i is the cutoff frequency and resonance R_i . The biquad coefficients and the SVF parameters are related as follows⁵:

$$\beta_{i,0}(f_i, m_i^{\text{LP}}, m_i^{\text{BP}}, m_i^{\text{HP}}) = f_i^2 m_i^{\text{LP}} + f_i m_i^{\text{BP}} + m_i^{\text{HP}}, \quad (10a)$$

$$\beta_{i,1}(f_i, m_i^{\text{LP}}, m_i^{\text{HP}}) = 2f_i^2 m_i^{\text{LP}} - 2m_i^{\text{HP}}, \quad (10b)$$

$$\beta_{i,2}(f_i, m_i^{\text{LP}}, m_i^{\text{BP}}, m_i^{\text{HP}}) = f_i^2 m_i^{\text{LP}} - f_i m_i^{\text{BP}} + m_i^{\text{HP}}, \quad (10c)$$

$$\alpha_{i,0}(f_i, R_i) = f_i^2 + 2R_i f_i + 1, \quad (10d)$$

$$\alpha_{i,1}(f_i, R_i) = 2f_i^2 - 2, \quad (10e)$$

$$\alpha_{i,2}(f_i, R_i) = f_i^2 - 2R_i f_i + 1. \quad (10f)$$

³The constant $1/\sqrt{2\pi}$ is introduced to satisfy Parseval's theorem. We derive equations with l_2 distance since our actual loss could make analysis intractable.

⁴The elementwise products are performed in the DFT domain. Therefore, more time-aliasing occurs in the form of circular convolution.

⁵We do not consider the time-domain realization and difference equation of the SVF since it does not matter under the LTI assumption.

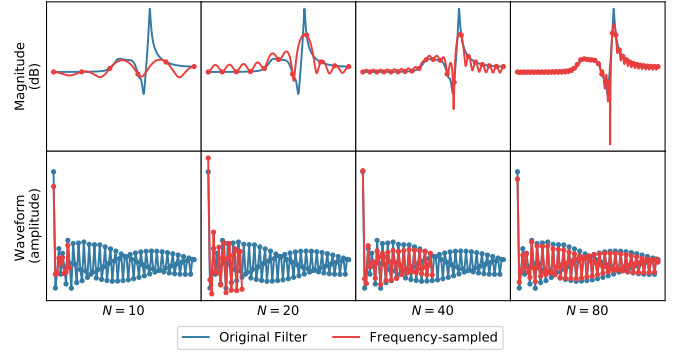


Fig. 2. FSM with various sampling resolutions. For visibility, H is set to an 8th-order IIR filter. Blue curves represent its magnitude response $|H(e^{j\omega})|$ (top row), and an IR $h[n]$ (bottom row) of H . Red curves represent frequency-sampled H , i.e., $|H_N(e^{j\omega})|$ and $h_N[n]$ for $N = 10, 20, 40$, and 80 (from left to right). $H_N(e^{j\omega})$ preserves the sampled points $(\omega_k, H(e^{j\omega_k}))$. The difference between $H(e^{j\omega})$ and $H_N(e^{j\omega})$ happens in-between the samples and gets smaller as N increases. $|H_N(e^{j\omega})|$ shows an oscillatory shape. Refer to Appendix A-B for their reasons. In the time domain, the length of $h_N[n]$ increases, and the time-aliasing error decreases as N increases.

In this paper, we SVF-parameterize every dense IIR filter H whose coefficients α_n, β_n are mostly nonzero; we use $f_i, R_i, m_i^{\text{LP}}, m_i^{\text{BP}}$, and m_i^{HP} as parameters of H and emphasize this by writing it as $\tilde{H}[k] = \prod_i (H_i^{\text{SVF}})_N[k]$ and calling H_i^{SVF} ‘‘SVF’’. It is because SVF has several advantages over the biquad.

- It is more interpretable yet still capable of expressing any arbitrary LTI filter [38].
- Unlike the biquad's parameters $\alpha_{i,0}, \alpha_{i,1}$, and $\alpha_{i,2}$, SVF parameters have independent stability conditions, $R_i > 0$ and $f_i > 0$, simplifying the design of nonlinear activations of a parameter estimator (refer to Section V-C) [16], [27].
- In our initial experiments, the proposed ARP estimation networks performed better with SVFs than biquads.

C. Differentiable Parametric Equalizer

Using the SVFs, we obtain a differentiable parametric equalizer (PEQ) as a special case of the differentiable IIR filter. PEQ is a serial composition of low-shelving H^{LS} , peaking H^{Peak} , and high-shelving filters H^{HS} . The components are second-order, and we obtain them by posing further constraints on each SVF [29]. With R and a new parameter G that gives $20 \log_{10}(G)$ dB gain, we parameterize $H^{\text{SVF}}(z; f, R, m^{\text{LP}}, m^{\text{BP}}, m^{\text{HP}})$ as

$$H^{\text{LS}}(z; f, R, G) = H^{\text{SVF}}(z; f, R, G, 2R\sqrt{G}, 1), \quad (11a)$$

$$H^{\text{Peak}}(z; f, R, G) = H^{\text{SVF}}(z; f, R, 1, 2RG, 1), \quad (11b)$$

$$H^{\text{HS}}(z; f, R, G) = H^{\text{SVF}}(z; f, R, 1, 2R\sqrt{G}, G). \quad (11c)$$

We use one low-shelving, one high-shelving, and $K-2$ peaking filters, i.e., $H^{\text{PEQ}}(z) = H^{\text{LS}}(z)H^{\text{HS}}(z) \prod_{i=1}^{K-2} H_i^{\text{Peak}}(z)$. Same as the differentiable IIR filter, a product of frequency-sampled components gives a differentiable PEQ.

IV. DIFFERENTIABLE ARTIFICIAL REVERBERATION

In this section, we derive differentiable FVN, ADV-FVN, and FDN. We first briefly review the original AR models. Then, we obtain their DAR counterparts by replacing the IIR components with FIRs using the FSM. Also, we modify the original models for efficient training and plausible reverberation.

A. Differentiable Filtered Velvet Noise

1) *Filtered Velvet Noise*: One can divide an arbitrary length- L RIR $h[n]$ into length- L_i segments $h_i[n]$ (total S segments without overlap, hence $L = \sum_{i=1}^S L_i$). Refer to Figure 3a for the visual illustration. Since reverberation is highly stochastic, we can model each $h_i[n]$ with a source noise $s_i[n]$ filtered with C_i . When a sparse signal named *velvet noise* $v_i[n]$ is used for each source, the source-filter decomposition of RIR becomes *Filtered Velvet Noise* (FVN) [11]. $v_i[n]$ has one nonzero value ± 1 in every length- T_i interval (therefore total L_i/T_i pulses), and each nonzero sample's sign and position are randomized. With low T_i (also called average pulse distance), $v_i[n]$ sounds smooth, preferable for modeling late reverberation [39], [40]. Even with high T_i , we can retain its smoothness with an allpass filter U_i . In short, each source is $s_i[n] = v_i[n] * u_i[n]$. Finally, since stochastic components cannot model direct arrival and early reflection $h_0[n]$, we add short deterministic FIR $\hat{h}_0[n]$. Therefore, an IR of FVN $\hat{h}[n]$ becomes

$$\hat{h}[n] = \hat{h}_0[n] + \sum_{i=1}^S \underbrace{v_i[n-d_i] * u_i[n] * c_i[n]}_{\hat{h}_i[n-d_i]}, \quad (12)$$

where each $d_i = \sum_{j=1}^{i-1} L_j$ is the delay length for the segment alignment ($d_1 = 0$). For efficient time-domain filtering, FVN comprises U_i with sparse Schroeder filters [41] (SAPs, $U_{i,j}^{\text{SAP}}(z) = (1 + \gamma_{i,j} z^{-\tau_{i,j}}) / (\gamma_{i,j} + z^{-\tau_{i,j}})$, where $\tau_{i,j}$ is the delay-line length and $\gamma_{i,j}$ is the feed-forward/back gain) and uses a low-order dense IIR filter as the ‘‘coloration filter’’ C_i .

2) *Differentiable Implementation*: We modify each FVN component to obtain differentiable FVN (refer to Figure 3a).

- *Velvet filter* V_i . To batch velvet segments of different FVN instances, we fix the nonuniform segmentation $\{L_i\}$. Then, we also fix the average pulse distance T_i of each V_i such that V_i combined with U_i sounds perceptually smooth.
- *Allpass filter* U_i . With fixed segmentation and echo density of V_i , we again tune and fix $\tau_{i,j}$ and $\gamma_{i,j}$ of each $U_{i,j}^{\text{SAP}}$. Since U_i is an IIR filter that bottleneck the training speed, we crop $u_i[n]$ to obtain its FIR approximation $\tilde{u}_i[n]$. The same collected FIRs \tilde{u} are used for every FVN instance.
- *Coloration filter* C_i . Our network estimates parameters of C_i for every FVN instance. Since C_i is an IIR filter, we accelerate the training by frequency-sampling $C_i(z)$ and converting it into a length- N FIR $(c_i)_N[n]$. We model C_i with K serial SVFs⁷, i.e., $C_i(z) = \prod_{k=1}^K C_{i,k}^{\text{SVF}}(z)$.

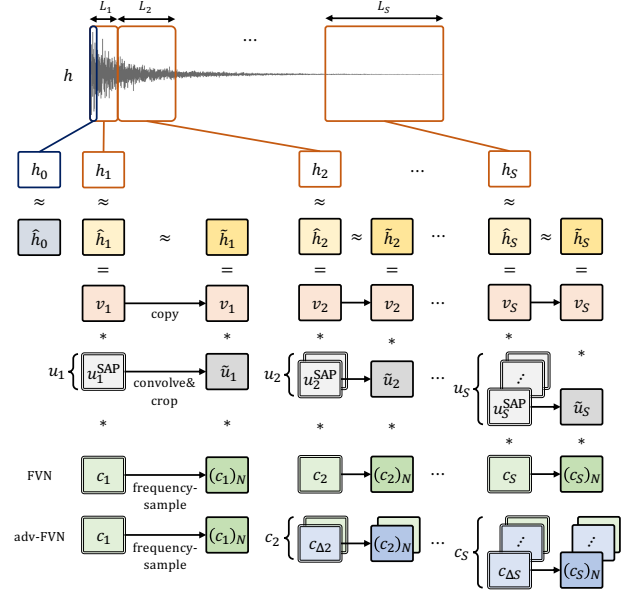
Therefore, IR of the differentiable FVN $\tilde{h}[n]$ becomes

$$\tilde{h}[n] = \hat{h}_0[n] + \text{overlap-add} \left\{ \underbrace{v_i[n] * \tilde{u}_i[n] * (c_i)_N[n]}_{\tilde{h}_i[n]} \right\}. \quad (13)$$

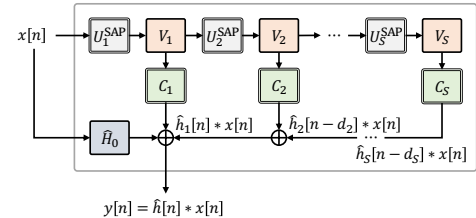
Since all $v_i[n]$, $\tilde{u}_i[n]$, and $(c_i)_N[n]$ are FIR, we can compute $\tilde{h}_i[n]$ efficiently by multiplying them in the frequency domain,

⁶We tuned L_i , T_i , $\tau_{i,j}$ and $\gamma_{i,j}$ to make FVN be computationally efficient and suppress perceptual artifact such as discontinuous or rough sound. In our initial experiment, estimating $\tau_{i,j}$ with a straight-through estimator (STE) [42] did not provide any performance gain over the manual parameter tuning.

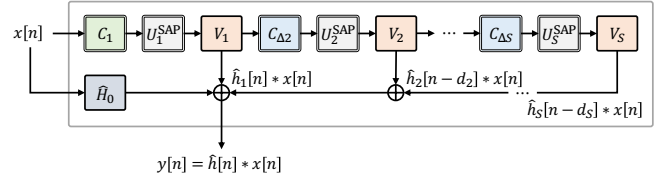
⁷All-pole constraint to C_i from the original work [11] is unnecessary since we do not use linear prediction.



(a) RIR modeling of modified FVN, ADV-FVN, and their differentiable implementation strategy.



(b) Modified FVN in the time domain.



(c) Modified ADV-FVN in the time domain.

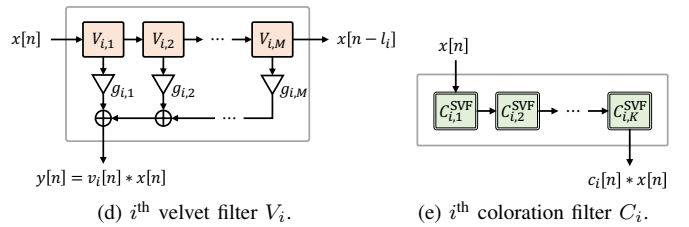


Fig. 3. FVN, ADV-FVN, and their differentiable implementations. (a) FVN and ADV-FVN divide a target RIR h into segments h_i and approximate each segment with $\hat{h}_i = v_i * u_i * c_i$, a velvet noise v_i filtered with an allpass filter U_i and a coloration filter C_i . We obtain the differentiable FVN and ADV-FVN by converting the IIR filters, U_i and C_i , into FIR filters into \tilde{u}_i and $(c_i)_N$ with manageable deviations. We emphasized the IIR filters with double border boxes in the figures. (b) Modified FVN. To retain a sharp transient, we inserting each SAP before its corresponding velvet filter. For each velvet filter V_i , an output with a down arrow is an input convolved with its velvet noise v_i . Another output with a right arrow is an L_i -sample-delayed input (refer to [11] for more details). (c) The same modification is performed to the ADV-FVN model. (d) For both FVN and ADV-FVN, each velvet filter V_i is divided into smaller velvet filters $V_{i,j}$ with different gain $g_{i,j}$. It is equivalent to dividing the velvet segments $v_i[n]$ into smaller segments $v_{i,j}[n]$ and multiplying each of them with $g_{i,j}$. (e) i^{th} coloration filter C_i in the time domain, which is serially connected SVF-parameterized biquads.

i.e., zero-pad followed by FFT, multiplication, and IFFT. Then, we can overlap-add $\tilde{h}_i[n]$ with conventional one-dimensional transposed convolutional layers.

3) *Modifications to the Original Model*: The original FVN was initially designed only for the analysis-synthesis task; it uses ground-truth direct arrival and early reflection cropped from the target RIR, i.e., $\hat{h}_0[n] = h_0[n]$, and only matches late reverberation. However, we also tackle the blind estimation task with FVN where $h_0[n]$ is not available; thus, to model the entire RIR better, we modify the original FVN as follows.

- *Finer segment gain*. We divide each $v_i[n]$ into M segments $v_{i,j}[n]$ of length $L_{i,j}$ without overlap ($\sum_{j=1}^M L_{i,j} = L_i$), then assign different gain $g_{i,j}$ to each of the segments, i.e., $v_i[n] = \sum_{j=1}^M g_{i,j} v_{i,j}[n - d_{i,j}]$ where $d_{i,j} = \sum_{k=1}^{j-1} L_{i,k}$ and $d_{i,1} = 0$. Figure 3d shows V_i in the time domain.
- *Cumulative allpass*. The original model smoothes every $v_i[n]$ with the same allpass U (serial SAPs) that smears any possible transient. Alternatively, we gradually smooth each $v_i[n]$ with $U_i = \prod_{j=1}^i U_j^{\text{SAP}}$. As illustrated in Figure 3b, U_i can be implemented in the time domain by inserting each U_j^{SAP} before V_j . Since we smooth the earlier segment less than the latter, we set smaller T_i to them.
- *Shorter deterministic component*. With the above changes, FVN can express the early RIR better with the stochastic segments; thus, we reduce the length of $\hat{h}_0[n]$.

4) *Implementation using a Deep-learning Framework*: Here we outline the generation procedure of $\tilde{\mathbf{h}}$, a batched tensor of multiple $\tilde{h}[n]$. Uniform segmentation $L_i = L$ is assumed for simpler demonstration. First, velvet segments are collected as a tensor $\mathbf{v} \in \mathbb{R}^{S \times M \times (L/M)}$ (we omit the batch axis). The sub-segment gains are also prepared as $\mathbf{g} \in \mathbb{R}^{S \times M}$. \mathbf{v} is multiplied with \mathbf{g} and filtered with the allpass filters $\tilde{\mathbf{u}} \in \mathbb{R}^{S, L_{\tilde{v}}}$, resulting in source segments $\tilde{\mathbf{s}} = \mathbf{v} \odot \mathbf{g} * \tilde{\mathbf{u}} \in \mathbb{R}^{S \times (L+L_{\tilde{v}}-1)}$ (broadcasting is performed). From the SVF parameters, \mathbf{f} , \mathbf{R} , \mathbf{m}^{LP} , \mathbf{m}^{BP} , and $\mathbf{m}^{\text{HP}} \in \mathbb{R}^{S \times K}$, we obtain the biquad coefficients, β and $\alpha \in \mathbb{R}^{S \times K \times 3}$, then calculate the frequency-sampled SVFs $\mathbf{C}_N^{\text{SVF}} \in \mathbb{C}^{S \times K \times (\lfloor N/2 \rfloor + 1)}$. Product of $\mathbf{C}_N^{\text{SVF}}$ along the SVF axis followed by IFFT gives the frequency-sampled coloration filters $\mathbf{c}_N \in \mathbb{R}^{S \times N}$. We convolve $\tilde{\mathbf{s}}$ and \mathbf{c}_N , then overlap-add it. Finally, adding deterministic FIR $\mathbf{h}_0 \in \mathbb{R}^Z$ gives the desired $\tilde{\mathbf{h}} \in \mathbb{R}^{S \times (L+L_{\tilde{v}}+N-2)}$. In the nonuniform segmentation case, we group adjacent velvet segments with the same L_i to a single tensor $\mathbf{v}_i \in \mathbb{R}^{S_i \times M \times (L_i/M)}$. Then, we follow the same procedure to obtain each $\tilde{\mathbf{h}}_i$ from \mathbf{v}_i and their ARP tensors. Finally, another overlap-add of $\tilde{\mathbf{h}}_i$ gives $\tilde{\mathbf{h}}$.

5) *Advanced Filtered Velvet Noise*: One can compose each coloration filter as $C_i(z) = C_1(z) \prod_{j=2}^i C_{\Delta j}(z)$, where C_1 is an initial coloration filter, and each $C_{\Delta j}$ is a delta-coloration filter added to the j^{th} source, respectively. With an assumption of gradual coloration change of reverberation, we can optimize FVN by setting the order of $C_{\Delta j}$ lower than C_1 's. Such a model is called *Advanced Filtered Velvet Noise (ADV-FVN)* [11]. Its time-domain implementation is illustrated in Figure 3c. We set C_1 and $C_{\Delta j}$ to be serial K_1 and K_{Δ} SVFs, respectively, which requires total $\bar{K} = K_1 + (S-1)K_{\Delta}$ SVFs. Naturally, the generation procedure of differentiable ADV-FVN differs from the differentiable FVN only at calculating \mathbf{c}_N . As shown at the

bottom of Figure 3a, we compute the cumulative product of \bar{K} SVFs $\mathbf{C}_N^{\text{SVF}} \in \mathbb{C}^{\bar{K} \times (\lfloor N/2 \rfloor + 1)}$, obtaining $\mathbf{C}_N \in \mathbb{R}^{\bar{K} \times (\lfloor N/2 \rfloor + 1)}$. Taking only $K_1 + (i-1)K_{\Delta}$ ($i = 1, \dots, K$) filters from \mathbf{C}_N with IFFT gives the desired $\mathbf{c}_N \in \mathbb{R}^{S \times N}$.

6) *Model Configuration Details*: Here we explain the exact configurations of our AR/DAR models used for the experiments. We found the following setups via comparisons, ablations, and informal listening tests. We primarily considered average match loss $\mathcal{L}_{\text{MATCH}}$ (refer to Section V-D) of a trained analysis-synthesis network for each AR model configuration. Each AR model's perceptual quality, interpretability, controllability, and computational efficiency, i.e., low floating-point operations per sample (FLOPs) were also considered.

We synthesize 2.5 seconds of IR (48kHz sampling rate, total $L = 120\text{k}$ samples) with FVN. We use $S = 20$ non-uniform velvet segments; their lengths L_i are $L/40$, $L/20$, and $L/10$ for 10, 5, and 5 segments, respectively, and their average pulse distances are $\mathbf{T} = [10, 20, 35, 50, 65, 90, 120, 135, 180, 220, 270, 320, 370, 420, 480, 540, 610, 680, 750, 820]$. The SAPs U_j^{SAP} are forced to have feed-forward gain $\gamma_j = 0.75 + 0.01j$ and delay $\tau = [23, 48, 79, 109, 113, 127, 163, 191, 229, 251, 293, 337, 397, 421, 449, 509, 541, 601, 641, 691]$. Each velvet segment has $M = 4$ sub-segments with different gains each and filtered with a coloration filter C_i with $K = 8$ SVFs. The differentiable FVN uses the FSM with $N = 4\text{k}$. The length of the deterministic FIR $h_0[n]$ is $Z = 50$. Our network estimates ARP tensors \mathbf{g} , \mathbf{f} , \mathbf{R} , \mathbf{m}^{LP} , \mathbf{m}^{BP} , \mathbf{m}^{HP} , and \mathbf{h}_0 , which are a total of 930 ARPs. The time-domain implementation \hat{H} (Figure 3b) requires 2166 FLOPs⁸.

For ADV-FVN, we set $K_1 = 8$ and $K_{\Delta} = 2$ to the initial coloration filter C_1 and each of the delta coloration filters $C_{\Delta j}$, respectively. Other hyperparameters are same to the FVN. Total 360 ARPs are estimated and \hat{H} requires 1511 FLOPs⁹.

B. Differentiable Feedback Delay Network

1) *Feedback Delay Network*: The most widely used class of AR models is the *delay network*, which recursively interconnects long delay lines [4]. Among numerous delay network models, we implement *Feedback Delay Network (FDN)* [12] differentially since it can express any other delay networks [28], [43]. Indeed, its difference equation can be expressed in a general delayed state-space form.

$$y[n] = \mathbf{C}^T \bar{\mathbf{y}}[n] + \hat{H}_0 x[n], \quad (14a)$$

$$\bar{\mathbf{y}}[n + \mathbf{d}] = \mathbf{A} \bar{\mathbf{y}}[n] + \mathbf{B} x[n]. \quad (14b)$$

That is, an input $x[n]$ is distributed and filtered with \mathbf{B}^{10} , then go through \mathbf{d} -sample parallel delay lines which are recursively

⁸Each modified velvet filter V_i requires gain M multiplications and $L_i/T_i - 1$ additions per output sample. With our S, L_i, T_i , and M , the total FLOPs required for the velvet filters are $\sum_{i=1}^S (L_i/T_i + M - 1) \approx 907$. Each SVF in transposed direct form II requires 5 multiplications and 4 additions per output sample, and $9SK = 1440$ FLOPs are required for the entire coloration filters. Each SAP requires 2 multiplications and additions; a total of $4K_{\text{U}} = 80$ FLOPs are required. The sum of the filtered segments requires $S - 1 = 19$ additions. Filtering the input with \hat{H}_0 and adding it to the wet output require $2Z = 100$ FLOPs. Therefore, the total FLOPs of our FVN are 2546.

⁹We need $9\bar{K} = 414$ FLOPs instead of 1440 for the coloration.

¹⁰We omit the curly bracket notation for the filtering operation, e.g., $H\{x[n]\}$, and simply write $Hx[n]$ for readability.

interconnected to themselves through a mixing filter matrix \mathbf{A} . The delay line outputs $\bar{y}[n]$ are filtered with \mathbf{C} and summed. We add a bypassed signal filtered with \hat{H}_0 to the summation, resulting in an output $y[n]$. Transfer function of FDN is

$$\hat{H}(z) = \mathbf{C}(z)^T (\mathbf{D}^{-1}(z) - \mathbf{A}(z))^{-1} \mathbf{B}(z) + \hat{H}_0(z) \quad (15)$$

where $\mathbf{D}(z) = \text{diag}(z^{-d})$ is a diagonal transfer function matrix (TFM) of shape $M \times M$ for the delay lines, i.e., $\mathbf{D}_{ii}(z) = z^{-d_i}$. $\mathbf{B}(z)$, $\mathbf{C}(z)$, and $\mathbf{A}(z)$ are input, output, and feedback TFM of shape $M \times 1$, $1 \times M$, and $M \times M$, respectively.

2) *Differentiable Implementation*: The FDN components, \mathbf{A} , \mathbf{B} , \mathbf{C} , and \mathbf{D} , are recursively interconnected such that, unlike FVN and ADV-FVN, one cannot divide its IR into independent segments and generate them separately. Instead, we frequency-sample its entire transfer function $\hat{H}(z)$ to obtain differentiable FDN $\tilde{H} = \hat{H}_N$. Obviously, \hat{H}_N is equivalent to a composition of individually frequency-sampled TFMs (FSTFMs), i.e.,

$$\tilde{h}[n] = \text{IFFT} \left\{ \mathbf{C}_N^T (\mathbf{D}_N^{-1} - \mathbf{A}_N)^{-1} \mathbf{B}_N + (\hat{H}_0)_N \right\} \quad (16)$$

where $\mathbf{D}_N = \text{diag}((z^{-d})_N) \in \mathbb{C}^{M \times M \times [N/2+1]}$ is an $M \times M$ diagonal FSTFM¹¹ of \mathbf{D} , i.e., $(\mathbf{D}_N)_{ii} = (z^{-d_i})_N \in \mathbb{C}^{[N/2+1]}$. Likewise, we can build \mathbf{B}_N , \mathbf{C}_N , and \mathbf{A}_N whose elements are frequency-sampled transfer functions of their original TFMs \mathbf{B} , \mathbf{C} , and \mathbf{A} , respectively. Each FSTFM is a batch of $[N/2+1]$ matrices; the matrix multiplications and inversions of equation (16) can be performed in parallel.

3) *Restrictions to the General Model*: Now it is obvious that we can derive a differentiable approximation of any FDN model (hence any delay network model). However, when following the general practice that uses many parallel delay lines (e.g., $M = 16$) for a high-quality reverberation, its differentiable model's FSTFMs consume too much memory, and their multiplications and inversions bottleneck the training speed. To tackle this, we reduce M and modify the components to make FDN plausible with low M . Refer to Figure 4 for its time-domain illustration.

- *Pre and Post Filter Matrix*. Following most previous works [19], [28], [44], \mathbf{B} is set to a (constant) gain vector \mathbf{b} . \mathbf{C} is composed of a gain vector \mathbf{c} and a common filter C_1 , i.e., $\mathbf{C} = C_1 \mathbf{c}$. C_1 is composed of serial K_{C_1} SVFs.
- *Feedback Filter Matrix*. While most FDN model combines channel-wise parallel delta-coloration (absorption) filters \mathbf{C}_Δ and an inter-channel mixing matrix \mathbf{Q} to compose the feedback filter matrix $\mathbf{A} = \mathbf{Q} \mathbf{C}_\Delta$, upon this, we also insert channel-wise allpass filters \mathbf{U} and apply *time-variance* to \mathbf{Q} . Then our feedback filter matrix is $\mathbf{A}_n = \mathbf{Q}_n \mathbf{U} \mathbf{C}_\Delta$.
- *Allpass Filters*. \mathbf{U} accelerates echo density build-up¹² [45]. Each channel of \mathbf{U} is composed of serial K_U SAPs, i.e., total $M \times K_U$ SAPs. Unlike the FVN and ADV-FVN, the

¹¹When H is an order- L FIR filter, one can obtain H_N without the FSM by shape-matching its IR $h[n]$ (zero-pad to length N if $L < N$ or manually applying time-aliasing with equation (5) if $L > N$) followed by FFT. Likewise, if a time-domain FIR matrix is given, one can compose its FSTFM by following the same procedure for each FIR element. While z^{-d} (therefore \mathbf{D}_N) can be calculated in such a way, we used the FSM because it bypasses unnecessary multiplication-with-zeros of FFT performed to the sparse FIR z^{-d_i} .

¹²For an FDN model with SAPs inserted in the feedback loop, its equivalent FDN model without SAPs exists and has higher M [28]; thus, our modification can be thought of as an FDN order compression method.

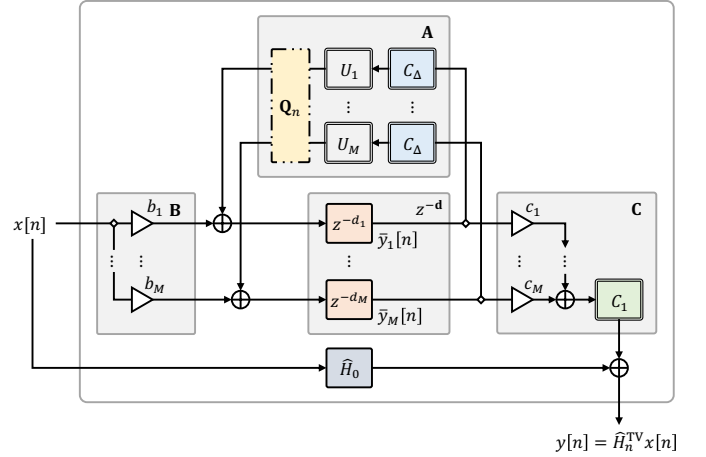


Fig. 4. Our modified FDN in the time domain. We restrict the fully general filter matrices to accelerate the training time and obtain an expressive, efficient, and controllable model. We simplify \mathbf{B} and \mathbf{C} to have only one coloration filter C_1 and use the same C_Δ for all feedback loops. A time-varying mixing matrix \mathbf{Q}_n and allpass filters \mathbf{U} are introduced to use FDN with small M (i.e., fast training) with minimal reverberation quality loss.

feed-forward/back gains γ of \mathbf{U} are variable parameters, and we estimate them with the network. Therefore, we frequency-sample \mathbf{U} for the differentiable model¹³.

- *Time-varying Mixing Matrix*. \mathbf{Q}_n reduces unnatural artifacts by modulating stationary poles of FDN. It is set to $\mathbf{Q}_n = \mathbf{Q}_0 \mathbf{R}^n$, where $\mathbf{Q}_0 = 2\mathbf{1}\mathbf{1}^T/M - \mathbf{I}$ is a Householder matrix, and \mathbf{R} is a tiny rotational matrix constructed from a random matrix [28], [43]. Since FSM is only applicable to LTI filters, we fix the mixing matrix to \mathbf{Q}_0 to obtain the differentiable model. With \mathbf{U} and \mathbf{Q}_n , FDN synthesizes plausible reverberation even with low M ¹⁴.
- *Absorption Filters*. Every channel of \mathbf{C}_Δ has the same filter C_Δ . Since \mathbf{Q}_n is unitary for every n , FDN is stable when $|C_\Delta(e^{j\omega})| < 1$ for all ω . C_Δ is a PEQ with K_{C_Δ} SVFs, which has simple stability conditions.
- *Bypass FIR*. H_0 is a length- Z FIR filter for the bypass. Since $Z \ll N$, we do not frequency-sample $H_0(z)$.

We summarize the modifications. The difference equation of our time-varying FDN \hat{H}_n^{TV} is

$$y[n] = C_1 \mathbf{c}^T \bar{\mathbf{y}}[n] + H_0 x[n], \quad (17a)$$

$$\bar{\mathbf{y}}[n + \mathbf{d}] = \mathbf{Q}_n \mathbf{U} \mathbf{C}_\Delta \bar{\mathbf{y}}[n] + \mathbf{b} x[n]. \quad (17b)$$

The transfer function of its LTI approximation $\hat{H}(z)$ is given as equation (15) with $\mathbf{B}(z) = \mathbf{b}$, $\mathbf{C}(z) = C_1(z) \mathbf{c}$, and $\mathbf{A}(z) = \mathbf{Q}_0 \text{diag}(\mathbf{U}_N(z) \odot \mathbf{C}_\Delta(z))$. Therefore, IFFT of

$$(C_1)_N \mathbf{c}^T (\mathbf{D}_N^{-1} - \mathbf{Q}_0 \text{diag}(\mathbf{U}_N \odot (\mathbf{C}_\Delta)_N))^{-1} \mathbf{b} \quad (18)$$

summed with $\hat{h}_0[n]$ gives an IR $\tilde{h}[n]$ of our differentiable FDN.

4) *Model Configuration Details*: $M = 6$ parallel delay lines have fixed delay lengths $\mathbf{d} = [233, 311, 421, 461, 587, 613]$ ¹⁵.

¹³Unlike the FVN and ADV-FVN case, trainable γ was found to be helpful for stable learning. Also, note that we do not modulate any parameters of \mathbf{U} since it could make the FDN unstable [28].

¹⁴We found that using *both* \mathbf{Q}_n and \mathbf{U} is crucial not only for better sound quality but also for a reduced gap between \hat{H} and \hat{H}^{TV} .

¹⁵Although we tried \mathbf{d} estimation by discretizing the network output to the nearest integer or prime and using STE for the training, it did not improve any performance.

$K_U = 4$ SAPs are used for each channel with fixed delay lengths $\tau = [[131, 151, 337, 353], [103, 173, 331, 373], [89, 181, 307, 401], [79, 197, 281, 419], [61, 211, 257, 431], [47, 229, 251, 443]]$. The tiny rotational matrix of the time-varying mixing matrix satisfies $\mathbf{R}^{30k} = \mathbf{I}$. Both C_1 and C_Δ use $K_{C_1} = K_{C_\Delta} = 8$ SVFs. Our FSTFMs have $N = 120k$ samples¹⁶. The order of the bypass FIR H_0 is $Z = 100$. We set the coloration filters' parameters \mathbf{f}_{C_1} , \mathbf{R}_{C_1} , $\mathbf{m}_{C_1}^{\text{LP}}$, $\mathbf{m}_{C_1}^{\text{BP}}$, $\mathbf{m}_{C_1}^{\text{HP}}$, \mathbf{f}_{C_Δ} , \mathbf{R}_{C_Δ} , and \mathbf{G}_{C_Δ} , gain vectors \mathbf{b} and \mathbf{c} , feed-forward/back gains γ of the SAPs, and coefficients of the bypass FIR \mathbf{h}_0 to the estimation targets (total 200 ARPs). \hat{H} and \hat{H}_n^{TV} require 889 and 1285 FLOPs, respectively¹⁷.

V. ARTIFICIAL REVERBERATION PARAMETER ESTIMATION WITH DIFFERENTIABLE ARTIFICIAL REVERBERATION

We first formally state the ARP estimation task. We aim to find an algorithm Φ that estimates ARPs \mathbf{P} of an AR model \hat{H} from target reverberation given in a certain form. If an RIR h is directly given, Φ and \hat{H} perform the *analysis-synthesis* task; the optimization objective of Φ is

$$\arg \min_{\Phi} \mathbb{E}_{h \sim \mathcal{D}_h} \left[\mathcal{L}(h, \hat{h}_{\mathbf{P}=\Phi(h)}) \right]. \quad (19)$$

In the above equation, $\mathcal{L}(\cdot, \cdot)$ is a loss or metric between two IRs. Since a ground-truth distribution \mathcal{D}_h of the real-world reverberation is unknown, it is replaced with a collection of simulated IRs or measured RIRs. Alternatively, when target reverberation is given indirectly as a reverberant signal $h * x$, i.e., dry source x sampled from \mathcal{D}_x and convolved with h , Φ and \hat{H} perform the *blind estimation* task.

$$\arg \min_{\Phi} \mathbb{E}_{h \sim \mathcal{D}_h, x \sim \mathcal{D}_x} \left[\mathcal{L}(h, \hat{h}_{\mathbf{P}=\Phi(h*x)}) \right]. \quad (20)$$

The blind estimation is an extension of the analysis-synthesis since $h * x = h$ when x is a unit impulse δ . However, we only consider x and \mathcal{D}_x of dry speech in this paper.

Using the differentiable model \hat{H} of the original H , we can train a DNN as an ARP estimator Φ with loss $\mathcal{L}(h, \hat{h})$. After the training, \hat{H} equipped with estimated ARPs, $\mathbf{P} = \Phi(h)$ or $\mathbf{P} = \Phi(x * h)$, can be used. We make the network architecture applicable to any task and AR/DAR model, as explained in the following subsections.

A. AR-Model-invariant Shared Encoder

The details of our ARP estimation network are as follows. As illustrated in Figure 1, it is composed of a model-invariant shared encoder that transforms an audio input (e.g., h or $h * x$) into a shared latent \mathbf{z} and ARP-groupwise layers that project \mathbf{z} into ARP tensors \mathbf{P}_i each. Refer to Table I for an overview.

Configuration of the shared encoder is fixed for every task and AR model. It takes a single-channel audio (2.5 seconds,

¹⁶Therefore, we synthesize 2.5 seconds of IR like the FVN and ADV-FVN model. However, a difference exists that IR of the true FDN model \hat{H} extends over the differentiable model's length N .

¹⁷Each component's FLOPs are as follows. \mathbf{b} and \mathbf{c} : $M = 6$. C_1 : $9K_1 = 72$. C_Δ : $9MK_1 = 432$. \mathbf{U} : $4MK_U = 96$. \mathbf{Q} : $M(2M - 1) = 66$. \hat{H}_0 : $2Z - 1 = 199$. Other adds: $2M = 12$. Matrix rotation: $M^2(2M - 1) = 396$. Sum of all FLOPs except for the rotation matrix gives 889 FLOPs; therefore, the time-varying model has $889 + 396 = 1285$ FLOPs.

TABLE I
ARCHITECTURE OF PROPOSED ARP ESTIMATION NETWORK.

LAYERS	OUTPUT SHAPE
INPUT	$\mathcal{B}_4, \mathcal{T}_{120k}$
LOG SPECTROGRAM	$\mathcal{B}_4, \mathcal{F}_{513}, \mathcal{T}_{938}$
CONV-2D (64, (7, 5), (1, 2)) + RELU	$\mathcal{B}_4, \mathcal{C}_{64}, \mathcal{F}_{507}, \mathcal{T}_{467}$
CONV-2D (128, (5, 5), (2, 1)) + RELU	$\mathcal{B}_4, \mathcal{C}_{128}, \mathcal{F}_{252}, \mathcal{T}_{463}$
CONV-2D (128, (5, 5), (2, 2)) + RELU	$\mathcal{B}_4, \mathcal{C}_{128}, \mathcal{F}_{124}, \mathcal{T}_{230}$
CONV-2D (128, (5, 5), (2, 2)) + RELU	$\mathcal{B}_4, \mathcal{C}_{128}, \mathcal{F}_{60}, \mathcal{T}_{113}$
CONV-2D (128, (5, 5), (1, 1)) + RELU	$\mathcal{B}_4, \mathcal{C}_{128}, \mathcal{F}_{56}, \mathcal{T}_{109}$
TRANSPOSE & RESHAPE	$\mathcal{B}\&\mathcal{T}_{436}, \mathcal{F}_{56}, \mathcal{C}_{128}$
BI-GRU $_{\mathcal{F}}$ (2, 64)	$\mathcal{B}\&\mathcal{T}_{436}, \mathcal{F}_{56}, \mathcal{C}_{128}$
TRANSPOSE & RESHAPE	$\mathcal{B}_4, \mathcal{T}_{109}, \mathcal{F}\&\mathcal{C}_{7168}$
BI-GRU $_{\mathcal{T}}$ (2, 128)	$\mathcal{B}_4, \mathcal{T}_{109}, \mathcal{F}\&\mathcal{C}_{256}$
DENSE + LAYERNORM + RELU	$\mathcal{B}_4, \mathcal{T}_{109}, \mathcal{F}\&\mathcal{C}_{256}$
DENSE + LAYERNORM + RELU	$\mathcal{B}_4, \mathcal{T}_{109}, \mathcal{F}\&\mathcal{C}_{256}$
PROJECTION LAYER FOR ARP TENSOR \mathbf{P}_i :	
TRANSPOSE & DENSE	$\mathcal{B}_4, \mathcal{F}\&\mathcal{C}_{256}, \mathcal{P}_{N_{i,1}}$
TRANSPOSE & DENSE & ACTIVATION	$\mathcal{B}_4, \mathcal{P}_{N_{i,1}}, \mathcal{P}_{N_{i,2}}$

48kHz sampling rate, total 120k samples) as an input. Next, the input is transformed into a log-magnitude spectrogram with a log-scaled frequency axis (from 20Hz to 24kHz). We prefer this frequency scale over the widely-used mel scale to preserve the resolution of the low-frequency band more. FFT size is set to 1024. We use the Hann window, and we slide it with 128 hop size. An "epsilon" 10^{-7} is added to the spectrogram before the log computation for numerical stability. The spectrogram goes through 5 stacked two-dimensional convolutional layers (CONV-2Ds), each followed by a rectified linear unit (RELU) activation. Then, bi-directional gated recurrent unit layers (BI-GRU) [46] are applied along the frequency axis (Bi-GRU $_{\mathcal{F}}$) and the time axis (Bi-GRU $_{\mathcal{T}}$) for a wider receptive field. Finally, following [25], dense (DENSE) layers, each followed by layer normalization (LAYERNORM) [47] and RELU activation, give the shared latent \mathbf{z} . This encoder has about 7M parameters.

In Table I, numbers inside the parentheses of CONV-2Ds indicate the number of output channels, kernel size, and stride size. Inside of the parentheses of BI-GRU, the number of layers and hidden units for each layer are written. $\mathcal{B}, \mathcal{C}, \mathcal{F}, \mathcal{T}$, and \mathcal{P} represent axes of output tensor for batch, channel, frequency, time, and parameter, respectively. Subscripted numbers are the sizes of the tensors along the axes.

B. ARP-groupwise Projection Layers

Now we aim to transform the two-dimensional shared latent $\mathbf{z} \in \mathbb{R}^{M_1 \times M_2}$ into each ARP tensor $\mathbf{P}_i \in \mathbb{R}^{N_{i,1} \times N_{i,2}}$, which is at most two-dimensional. We also consider the one-dimensional tensors as two-dimensional with $N_{i,1} = 1$ or $N_{i,2} = 1$. Then, we compose each projection layer with two axis-by-axis shape-matching dense layers. That is, we first transpose and apply an M_1 -to- $N_{i,1}$ dense layer to \mathbf{z} to obtain an $M_2 \times N_{i,1}$ tensor. Then, applying another transpose and M_2 -to- $N_{i,2}$ dense layer to the intermediate tensor gives the desired shape. We do not use nonlinear activation between the dense layers. This approach factorizes a single large $M_1 M_2$ -to- $N_{i,1} N_{i,2}$ dense layer into

two smaller layers, reducing the number of parameters from $N_{i,1}N_{i,2}(M_1M_2 + 1)$ to $N_{i,1}(M_1 + 1) + N_{i,2}(M_2 + 1)$. Refer to the lower part of Table I for a summary. The shape of \mathbf{z} is 109×256 , and our FVN, ADV-FVN, and FDN model used for the experiment and evaluation have ARP tensors of shape listed in Table II. Their projection layers have about a total of 30k, 68k, and 30k parameters, respectively.

C. Nonlinear Activation Functions and Bias Initialization

Each ARP group has different stability conditions and desired distribution. To satisfy these, we attach a nonlinear activation function to each projection layer’s last dense layer and initialize its bias as follows. Refer to Table II for a summary.

1) Nonlinear Activation Functions:

- For the resonance \mathbf{R} of the SVF, we use scaled softplus $\log(1 + e^x)/\log(2)$ to center the initial distribution at 1 and satisfy the stability condition $\mathbf{R} > \mathbf{0}$.
- For the cutoff \mathbf{f} , we use $\tan(\pi\sigma(x)/2)$ to ensure $\mathbf{f} > \mathbf{0}$ where $\sigma(x) = 1/(1 + e^{-x})$ is logistic sigmoid. $\pi\sigma(x)/2$ represents normalized cutoff frequency $\pi\omega/\omega_s$.
- We use activation 10^x for PEQ components’ gains \mathbf{G} . The pre-activation x gives $20x$ dB gain for each component.
- For the PEQs of FDN’s delta-coloration filters, we ensure the magnitude response of each component smaller than 1 such that $|C_\Delta(e^{j\omega})| < 1$ holds. We achieve the condition using $10^{-\zeta(x)}$ for \mathbf{G} , which gives negative decibel gain at the center frequency. For the shelving filters, $R > \sqrt{2}/2$ is also required to prevent their magnitude responses “spike” higher than 1; thus, we add $\sqrt{2}/2$ to the softplus activation.
- For the feed-forward/back gains γ of channel-wise allpass filters \mathbf{U} inside FDN, we use sigmoid activation $\sigma(x)$ ¹⁸.

2) Bias Initialization:

- We initialize bias of the \mathbf{f} projection layer to $\sigma^{-1}(2\omega_k/\omega_s)$ where each ω_k is desired initial cutoff frequency of k^{th} SVF. We set $\omega_k = \omega_{\min}(\omega_{\max}/\omega_{\min})^{(k-1)/(K-1)}$ such that the frequencies are equally spaced in the logarithmic scale from $\omega_{\min} = 40\text{Hz}$ to $\omega_{\max} = 12\text{kHz}$. For SVFs inside the ADV-FVN’s initial/delta-coloration filters, we perform random permutation to the frequency index k , resulting in new index \tilde{k} to prevent SVFs for latter segments having higher initial center frequencies.
- Decoder biases of the SVF mixing coefficients, \mathbf{m}^{LP} , \mathbf{m}^{BP} , and \mathbf{m}^{HP} , are initialized to 1, 2, and 1, respectively, such that initial magnitude responses of SVFs slightly deviate from 1. This prevents the vanishing/exploding magnitude of the serial SVFs and the network’s loss gradients.
- For PEQ gains \mathbf{G} of FDN’s delta-coloration filters, we set each of their biases to -10 such that FDN’s initial IR has long enough reverberation time.

D. Loss Function

1) *Match Loss*: We compare the estimation and the ground-truth with a match loss $\mathcal{L}_{\text{MATCH}}$, a modified multi-scale spectral loss from [25]. We calculate l_1 (absolute) distances between

¹⁸While $-1 < \gamma < 1$ is the full stability condition, we found that either $0 < \gamma < 1$ or $-1 < \gamma < 0$ is sufficient for the reverberation quality.

TABLE II
TARGET ARP TENSORS AND THEIR NONLINEAR ACTIVATION FUNCTIONS AND BIAS INITIALIZATIONS FOR EACH AR MODEL.

MODEL	COMP.	ARP	SHAPE	ACTIV.	BIAS.
FVN	$s_i[n]$	\mathbf{g}	$S_{20} \times M_4$		
	C_i	\mathbf{f}	$S_{20} \times K_8$	$\tan(\frac{\pi\sigma(x)}{2})$	$\sigma^{-1}(\frac{2\omega_k}{\omega_s})$
		\mathbf{R}	$S_{20} \times K_8$	$\frac{\zeta(x)}{\zeta(0)}$	
		\mathbf{m}^{LP}	$S_{20} \times K_8$		1
		\mathbf{m}^{BP}	$S_{20} \times K_8$		2
\mathbf{m}^{HP}	$S_{20} \times K_8$		1		
H_0	\mathbf{h}_0		Z_{50}		
ADV-FVN	$s_i[n]$	\mathbf{g}	$S_{20} \times M_4$		
	$C_1, C_{\Delta j}$	\mathbf{f}	\bar{K}_{46}	$\tan(\frac{\pi\sigma(x)}{2})$	$\sigma^{-1}(\frac{2\omega_k}{\omega_s})$
		\mathbf{R}	\bar{K}_{46}	$\frac{\zeta(x)}{\zeta(0)}$	
		\mathbf{m}^{LP}	\bar{K}_{46}		1
		\mathbf{m}^{BP}	\bar{K}_{46}		2
\mathbf{m}^{HP}	\bar{K}_{46}		1		
H_0	\mathbf{h}_0		Z_{50}		
FDN	\mathbf{B}	\mathbf{b}	M_6		
	\mathbf{C}	\mathbf{c}	M_6	$\tan(\frac{\pi\sigma(x)}{2})$	$\sigma^{-1}(\frac{2\omega_k}{\omega_s})$
		\mathbf{R}_{C_1}	$K_{C_1 8}$	$\frac{\zeta(x)}{\zeta(0)}$	
		$\mathbf{m}_{C_1}^{\text{LP}}$	$K_{C_1 8}$		1
		$\mathbf{m}_{C_1}^{\text{BP}}$	$K_{C_1 8}$		2
$\mathbf{m}_{C_1}^{\text{HP}}$	$K_{C_1 8}$		1		
\mathbf{A}	\mathbf{f}_{C_Δ}	$K_{C_\Delta 8}$	$\tan(\frac{\pi\sigma(x)}{2})$	$\sigma^{-1}(\frac{2\omega_k}{\omega_s})$	
	\mathbf{R}_{C_Δ}	$K_{C_\Delta 8}$	$\zeta(x) + \frac{\sqrt{2}}{2}$		
	\mathbf{G}_{C_Δ}	$K_{C_\Delta 8}$	$10^{-\zeta(x)}$	-10	
	γ	$M_6 \times K_{u4}$	$\sigma(x)$		
H_0	\mathbf{h}_0		Z_{100}		

two magnitude spectrograms and sum altogether. We use the FFT sizes of 256, 512, 1024, 2048, and 4096, and the frequency axes are log-scaled like the encoder’s. Hop sizes are 25% of their respective FFT sizes, and Hann windows are used.

$$\mathcal{L}_{\text{MATCH}}(h, \tilde{h}) = \sum \|\text{STFT}(h) - \text{STFT}(\tilde{h})\|_1. \quad (21)$$

2) *Regularization*: We regularize the FVN and ADV-FVN networks to reduce their frequency-sampled coloration filters’ time-aliasing. As shown in equation (6) and (7), pole radii affect the reliability of the frequency-sampled filter (hence DAR model) and its parameter estimator. Since each individual SVF’s IR $(c_{i,k}^{\text{SVF}})_N[n]$ can be computed, we encourage reducing its pole radii by penalizing the IR’s decreasing speed. Each decreasing speed $\gamma_{i,k}$ is calculated by the ratio of the average amplitude of first and last n_0 samples of $(c_{i,k}^{\text{SVF}})_N[n]$. We fix n_0 to $N/8$. Then, each $\gamma_{i,k}$ is weighted with softmax along the SVF-axis to penalize higher $\gamma_{i,k}$ more and summed.

$$\gamma_{i,k} = \frac{\sum_{n=N-n_0}^N |(c_{i,k}^{\text{SVF}})_N[n]|}{\sum_{n=0}^{n_0} |(c_{i,k}^{\text{SVF}})_N[n]|}, \quad (22a)$$

$$\mathcal{L}_{\text{REG}} = \sum_{i=1}^S \frac{\sum_{k=1}^K \gamma_{i,k} e^{\gamma_{i,k}}}{\sum_{j=1}^K e^{\gamma_{i,j}}}. \quad (22b)$$

We omit \mathcal{L}_{REG} for the FDN networks¹⁹. We batch 4 IRs and average their losses. Therefore, our full loss function \mathcal{L} is

$$\mathcal{L}(\mathbf{h}, \tilde{\mathbf{h}}) = \mathcal{L}_{\text{MATCH}}(\mathbf{h}, \tilde{\mathbf{h}}) + \beta \mathcal{L}_{\text{REG}}(\mathbf{c}_N^{\text{SVF}}) \quad (23)$$

where $\beta = 1$ for FVN and ADV-FVN and $\beta = 0$ for FDN.

VI. EXPERIMENTAL SETUP

A. Data

1) *Room Impulse Response*: We generated target RIRs for the training with shoebox room simulations based on the image-source method [48], [49]. We randomized room parameters such as room size, each wall’s frequency-dependent absorption coefficient, air temperature/humidity, and source/microphone position for each simulation to reflect various acoustic environments. We generated a total of 200k RIRs and used them for the training²⁰. We collected real-world measured RIRs from OpenAIR [50], ACE Challenge [51], and a private dataset²¹ for the evaluation. We split a total of 1835 RIRs into validation (836) and test set (999), ensuring that each set consists of RIRs from different rooms. We performed following processing steps for each RIR before the training.

- We cropped the onset of each RIR so that it immediately starts with the direct arrival. We detected the onset using the mean-over-time method [52].
- Then, we multiplied random gain to the first 5ms of the IR to diversify the network input.
- Finally, we normalized the energy of the IR to 1.

2) *Reverberant Speech*: We used the VCTK dataset [53] for dry speech. We split it into the train (61808), validation (21608), and test (4912) set so that each set is composed of the speech recordings from different speakers. We normalized every speech sample to have root-mean-square (RMS) energy of -20 dB. We sampled an RIR and a dry speech sample from their respective datasets and convolved them to generate a reverberant speech sample. We random-selected a 2.5-second segment from it for the input.

B. Training

We used Adam optimizer [54] for the training. We set the initial learning rate to 10^{-4} for FVN and ADV-FVN and 10^{-5} for FDN. For FDN, gradients were clipped to ± 10 before the parameter update for stable training. After five epochs (we count an epoch with the IR training set), we decayed the learning rate. For the analysis-synthesis networks, we multiplied $10^{-0.2}$ every epoch for five epochs. For the blind estimation or both-performing networks, $10^{-0.1}$ was multiplied for ten epochs. We finished the training if the train/validation loss converge, which took no more than 20 epochs for the analysis-synthesis networks and 30 epochs for the other networks.

¹⁹With FDN, time-aliasing is inevitable to match the target with reverberation time longer than N . Also, unlike FVN and ADV-FVN, our networks’ estimation always remained in marginally stable regions without any regularisation.

²⁰On-the-fly generation of every training IR with randomization could yield the best and most robust network performance. However, even with shoebox restriction, which accelerates the IR computation with the image-source method, since the simulation of a room with long reverberation time requires high-order images, it bottlenecks the training speed.

²¹It has IRs measured from a more diverse set of spaces than the OpenAIR and ACE Challenge dataset.

C. Evaluation Metrics

We evaluated the performance of our networks with the match loss ($\mathcal{L}_{\text{MATCH}}$) and reverberation parameter differences (RPDs), i.e., reverberation time T_{30} , direct-to-reverberant ratio DRR, and clarity C_{50} difference [55], [56]. We report both full-band difference (FULL) and average differences measured at octave bands of center frequencies 125, 250, 500, 1k, 2k, 4k and 8kHz (FREQ). Since our DAR models only generate 2.5 seconds of target IR, we calculated the RPDs with the cropped ground-truth IR.

To estimate the perceptual distance between two reverberations, we can compare their RPDs with their respective Just Noticeable Differences (JNDs) [8]. Reported JNDs of T_{30} from previous works vary from 5% [57] up to about 25% [58]. For C_{50} , 1dB [59] and 1.1dB [60] were reported. [61] found that DRR’s JND depends on its value: 6dB at -10 dB, 2dB at 0dB, 3dB at 10dB, and 8dB at 20dB.

D. Energy Decay Relief Contours

We also evaluated the performance with energy decay relief (EDR) contour plots. EDR calculates the remaining frequency-dependent energy of an IR h at a given time. It can be obtained via reverse integration of its frequency-dependent energy along the time axis as follows [19],

$$\text{EDR}(m, n) = \sum_{i=n}^{\infty} |S(m, i)|^2, \quad (24)$$

where $S(m, n) = \text{STFT}(h)$ is a spectrogram of h , and m and n denote frequency bin index and time frame index, respectively. While the original EDR plot has a three-dimensional “waterfall” shape, we transformed it into a two-dimensional contour plot regarding the energy value as height for visibility. Then, by overlaying contour plots of multiple IRs, e.g., a target and its estimation, we can compare their frequency-dependent decay.

VII. EVALUATION RESULTS

We report evaluation results of the ARP estimation networks. We trained each network Φ with every proposed DAR model for the three tasks: analysis-synthesis (AS), blind estimation (BE), and both tasks (BOTH). This section denotes each network with Φ subscripted with its AR/DAR model and superscripted with its target task, e.g., $\Phi_{\text{FVN}}^{\text{AS}}$. We denote multiple networks for the same task or AR/DAR model with a dash, e.g., $\Phi_{\text{FVN}}^{\text{AS}}$ denotes $\Phi_{\text{FVN}}^{\text{AS}}$, $\Phi_{\text{ADV-FVN}}^{\text{AS}}$, and $\Phi_{\text{FDN}}^{\text{AS}}$.

Table III shows the average match loss with the DAR models $\mathcal{L}_{\text{MATCH}}(h, \tilde{h})$ and the AR models $\mathcal{L}_{\text{MATCH}}(h, \hat{h})$ separately. For BOTH networks $\Phi_{\text{FDN}}^{\text{BOTH}}$, we report their AS and BE performance separately. For Φ_{FDN}^- , although the time-varying model H_n^{TV} does not have an IR, we fed a unit impulse δ to it to obtain its response $\hat{h}^{\text{TV}} = \hat{H}^{\text{TV}}\{\delta\}$ and calculate $\mathcal{L}_{\text{MATCH}}(h, \hat{h}^{\text{TV}})$ for evaluation. To cover the time-varying model’s various states, we initialized the mixing matrix to $\mathbf{Q} = \mathbf{Q}_0 \mathbf{R}^m$, where m is an integer sampled from $[0, 30k)$. For Φ_{FVN}^- and $\Phi_{\text{ADV-FVN}}^-$, we report their DAR estimation losses (subscripted) and true LTI losses in the $\mathcal{L}_{\text{MATCH}}$ column, from left to right, respectively. For Φ_{FDN}^- , we provide their DAR, LTI, and LTV loss (from

TABLE III
ARP ESTIMATION RESULTS ON VARIOUS TASKS AND DAR MODELS.

MODEL	TASK		$10^{-1}\mathcal{L}_{\text{MATCH}}$	T_{30} (%)				DRR (dB)				C_{50} (dB)			
	TRAIN	TEST		FULL		FREQ		FULL		FREQ		FULL		FREQ	
FVN	AS		1.236 1.236	1.79	1.89	4.26	4.20	0.92	0.94	3.41	3.39	0.56	0.60	1.94	1.95
	BE		1.436 1.437	9.23	9.12	11.60	11.73	2.04	2.01	4.34	4.29	0.93	0.93	2.37	2.34
	BOTH	AS	1.351 1.350	2.88	2.92	8.84	8.74	1.38	1.39	3.71	3.76	0.64	0.67	2.13	2.13
		BE	1.450 1.450	12.96	13.06	16.41	16.39	2.27	2.30	4.49	4.54	0.99	0.98	2.33	2.34
ADV-FVN	AS		1.275 1.277	4.06	4.77	9.67	9.96	1.61	1.59	3.72	3.64	0.62	0.61	2.08	2.06
	BE		1.436 1.437	9.65	9.57	12.50	12.47	2.30	2.31	4.20	4.16	1.22	1.21	2.35	2.34
	BOTH	AS	1.407 1.407	6.51	6.16	9.11	9.07	1.36	1.39	4.16	4.19	0.60	0.62	2.72	2.77
		BE	1.442 1.441	10.11	9.91	12.52	12.41	2.31	2.28	4.58	4.68	1.10	1.15	2.63	2.63
FDN	AS		1.277 1.307 1.334	5.60	5.93	8.47	11.86	12.48	11.59	1.78	1.81	1.71	3.80	3.93	3.83
	BE		1.428 1.436 1.484	15.04	15.38	13.26	18.08	18.10	15.62	4.16	4.16	3.93	6.76	6.77	6.56
	BOTH	AS	1.386 1.387 1.399	7.34	7.34	7.43	9.06	9.06	9.60	2.06	2.06	2.28	5.36	5.36	5.45
		BE	1.436 1.439 1.453	15.08	15.09	13.91	16.19	16.23	15.60	3.74	3.74	3.90	6.63	6.62	6.69
RANDOM RIR PAIRS			3.041	66.65		68.26		4.61		6.31		5.10		6.33	

left to right, with the first two subscripted). Also, we similarly report each network’s median RPD results. Finally, we report the evaluation metrics calculated with randomly sampled RIR pairs as a performance lower bound.

Figure 5 visualizes estimations of Φ_{-}^{AS} by showing overlaid EDR contour plots for every target RIR h , its DAR estimation \tilde{h} , AR estimation \hat{h} , and the response of the time-varying model \hat{h}^{TV} of FDN. The first three columns and the others illustrate estimations results where targets are from the train (simulated) IRs and the test (real-world) RIRs, respectively. Figure 6 shows the magnitude responses of each coloration filter and its SVFs, whose parameters are estimated with Φ_{-}^{AS} .

A. Reliability of the DAR Models

Each differentiable approximation \tilde{H} has to be close to its original AR model \hat{H} to make the trained networks reliable. As reported in Table III, $\mathcal{L}_{\text{MATCH}}$ and RPD differences between \tilde{H} and \hat{H} are much smaller than metrics calculated with the RANDOM RIR PAIRS. While the random pair has an average $\mathcal{L}_{\text{MATCH}}$ of 3.041×10^{-1} , the deviation of average $\mathcal{L}_{\text{MATCH}}$ due to the FSM is at most 10^{-4} for Φ_{-}^{FVN} , 2×10^{-4} for $\Phi_{-}^{\text{ADV-FVN}}$, and 3.0×10^{-3} for Φ_{-}^{FDN} . The Φ_{-}^{FDN} , show more deviation than others since FDN sometimes frequency-samples an entire IR whose reverberation time is longer than N , which leads to more severe time-aliasing. Adding time-variance to the LTI model \hat{H}_n^{TV} degrades $\mathcal{L}_{\text{MATCH}}$ more, which is at most 5.7×10^{-3} . Yet, it is negligible compared to the random RIR pair value. Similarly, median RPD deviations due to the differentiable approximation are small compared to the lower bound references.

EDR contour plots in Figure 5 also support such reliability by showing that the contour plots of \tilde{h} , \hat{h} , and \hat{h}^{TV} are very close to each other. If differences exist, they are mostly in low-energy regions, which makes them perceptually unnoticeable.

B. Performance Difference Between Target Tasks

Without surprise, Φ_{-}^{AS} showed better performances in most metrics than Φ_{-}^{BE} and Φ_{-}^{BOTH} . Again, refer to Figure 5 for their estimation results of Φ_{-}^{AS} . However, their performance slightly

degrades with real-world RIRs from the test set, which implies that distributions of the simulated IRs and real-world RIRs are different. Still, they estimate high-energy regions accurately.

Compared to Φ_{-}^{AS} , Φ_{-}^{BE} perform relatively worse; their match loss and RPD values are marginally higher than those of Φ_{-}^{AS} . It is because their encoders have an additional burden to implicitly retrieve target reverberation h from a given reverberant speech $h*x$, which is more challenging. Likewise, Φ_{-}^{BOTH} show slightly degraded results than the single-task-performing counterparts²².

C. Performance Difference Between AR Models

Each AR model approximates target reverberation differently, which is a deliberate design choice. Consequently, the networks’ performance also varies according to their attached AR model.

FVN has an independent coloration filter C_i for each source segment $s_i[n]$ (see Figure 6 for the visualizations). With such flexibility, its network for each task, Φ_{-}^{AS} , Φ_{-}^{BE} , and Φ_{-}^{BOTH} , outperforms the other AR models’ counterparts. However, it has the largest number of ARPs (930) among experimented AR models, which makes it cumbersome to control the parameters manually. It also has the highest FLOPs (2546), which could be computationally heavy for real-time filtering of multiple FVN instances. Instead, ADV-FVN optimizes each C_i as the initial coloration filter C_1 combined with the delta-coloration filters $C_{\Delta j}$, which makes the model more controllable and efficient (360 ARPs and 1511 FLOPs) than FVN. Without surprise, such simplification costs estimation performance. Because the underlying assumption of the filter optimization that coloration of a real-world RIR changes gradually does not necessarily hold, Φ_{-}^{AS} reports increased FREQ RPD values compared to Φ_{-}^{AS} (e.g., T_{30} from 4.20 to 9.96). In addition, $\Phi_{-}^{\text{ADV-FVN}}$ are more challenging to optimize than Φ_{-}^{FVN} since the coloration of each segment depends on the previous one. Indeed, their training losses decreased slower than Φ_{-}^{AS} . FDN has an even

²²Exceptions exist: while Φ_{-}^{BOTH} and Φ_{-}^{FDN} showed higher $\mathcal{L}_{\text{MATCH}}$ on the AS task than $\Phi_{-}^{\text{ADV-FVN}}$ and Φ_{-}^{AS} , respectively, some of their RPDs were better than their counterparts. For example, Φ_{-}^{FDN} showed 9.60 FREQ T_{30} while Φ_{-}^{AS} showed 11.59 FREQ T_{30} .

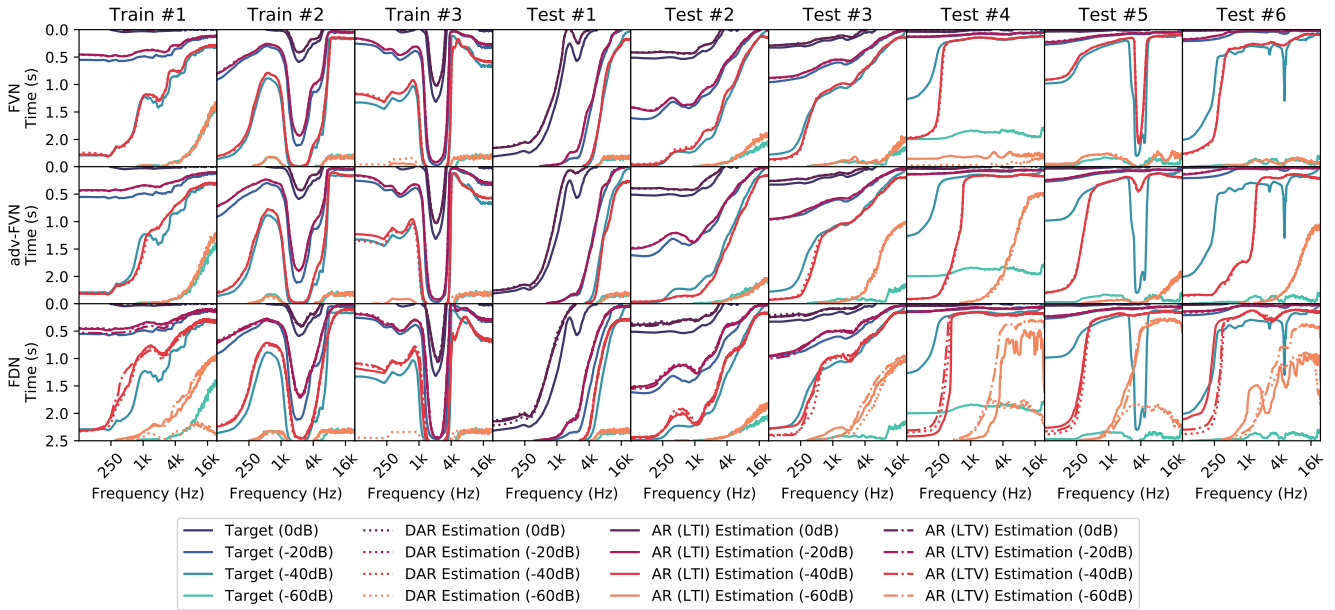


Fig. 5. Overlaid EDR contour plots of the target RIRs and their estimations with the trained FVN (top row), ADV-FVN (middle row), and FDN (bottom row) analysis-synthesis networks. Plots on the same column show the same target RIR h (blue curves). For each h , each network’s estimations are drawn in its respective plot. With the estimated ARPs, we plotted the EDR contour plot of the AR model’s IR \hat{h}_P (red curves, dotted), and the additional time-varying model’s response \hat{h}_P^V (red curves, dash-dotted) for FDN. The latter three are very similar to each other, showing that the FSM is a reliable method. The first three and the other columns’ target RIRs are simulated IRs and real-world RIRs (sampled from the test set), respectively. While estimations for the real-world RIR deviated slightly more than the simulated ones, they still captured the frequency-dependent reverberation decay of the high-energy region well. The right three columns’ target RIRs were deliberately chosen to illustrate the poor-performing examples and the differences between the AR models. While FVN successfully reconstructed the unseen radical frequency-dependent decay, others struggled to do so.

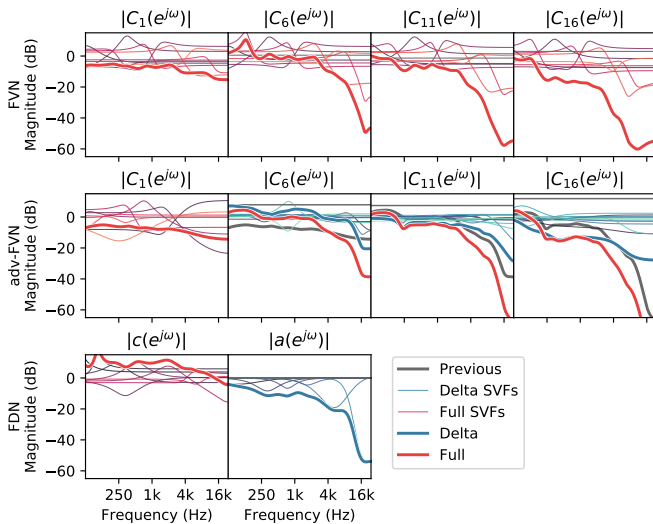


Fig. 6. Magnitude responses of the coloration filters of the AR models. The filters’ parameters were estimated with the trained analysis-synthesis networks. Each top, middle, and bottom row represents the FVN, ADV-FVN, and FDN models, respectively. For the FVN and ADV-FVN model, we selectively plotted the $i = 1, 6, 11,$ and 16^{th} filters C_i for visibility. The thick and thin curves represent the full coloration filters and their SVF components, respectively. The red curves represent C_i assigned to the source segments. Each thin grey line represents an average gain for each source segment. For ADV-FVN, the blue curves represent the delta-coloration filters $C_{\Delta j}$. Also, the previous colorations are drawn with the thick grey curves to emphasize the effects of the delta-colorations. Since T_i of source segment increases, their filters’ overall gain does not need to change much; we compensated such energy decrease for more intuitive visualization. For FDN, the red and blue curves represent the initial coloration C_1 and the feedback filter C_{Δ} , respectively. Note that the total energy of C_1 of FDN is higher than the initial coloration filters of FVN and ADV-FVN because of its lower source energy than the other models.

more optimized structure by using a single delta-coloration filter C_{Δ} for each outer feedback loop. Like ADV-FVN, FDN trade-offs performance of its estimators Φ_{FDN}^- with its controllability and computational efficiency (200 ARPs and 1285 FLOPs). Again, the estimation performance degradation comes from the FDN’s restricted expressibility (forced exponential decay) and training difficulty.

VIII. CONCLUSION

In this work, we proposed DAR models that can be integrated with modern DNNs end-to-end. Among many possible DAR models, we selectively derived differentiable FVN, ADV-FVN, and FDN. However, the suggested strategy for obtaining the differentiable model, i.e., replacing the IIR components with the FIR approximations using the FSM, could be applied to any other AR model and LTI filter. We applied the DAR models to the analysis-synthesis and blind estimation task. The evaluation results showed that the proposed ARP estimation networks attached with the DAR models could capture target reverberation accurately without custom engineering for each AR/DAR model and task. Furthermore, we investigated how each AR/DAR model can be compared in terms of its expressive power and difficulties of parameter optimization under the deep-learning environment. We have found a trade-off relationship between the estimation performance and compactness of the AR/DAR model’s structure. For example, although the FVN-equipped networks performed better than the others, FVN also has the largest ARPs and the highest FLOPs. Seeking for more “deep-learning-friendly” AR/DAR models and “AR/DAR-friendly” DNNs are left as future work.

APPENDIX A

DETAILS ON THE FREQUENCY-SAMPLING METHOD

A. Proof of the Equation 5

If a causal, stable LTI filter H has $H(z) = \sum_{n=0}^{\infty} h[n]z^{-n}$, then $H_N[k] = (\sum_{n=0}^{\infty} h[n]z^{-n})_N[k] = \sum_{n=0}^{\infty} h[n](z^{-n})_N[k]$ holds. Since each frequency-sampled n -sample delay $(z^{-n})_N$ is N -periodic, i.e., $(z^{-n\%N})_N = (z^{-n})_N = e^{-j2\pi k(mN+n)/N}$, the summation becomes $\sum_{m=0}^{\infty} \sum_{n=0}^{N-1} h[mN+n](z^{-n})_N[k] = \sum_{n=0}^{N-1} \sum_{m=0}^{\infty} h[mN+n]e^{-j2\pi kn/N}$, i.e., DTFT of a length- N signal $h_N[n] = \sum_{m=0}^{\infty} h[mN+n](u[n] - u[n-N])$.

B. Time-aliasing in the Frequency Domain

For a complete discussion on the time-aliasing, we address its effect in the frequency domain. First, inverse DFT of $H_N[k]$ is $h_N[n] = \sum_{k=0}^{N-1} H_N[k]e^{j\omega_k}(u[n] - u[n-N])/N$. Its frequency response is then $H_N(e^{j\omega}) = \sum_{k=0}^{N-1} H_N[k]\kappa(e^{j(\omega-\omega_k)})$, where $\kappa(e^{j\omega})$ is a phase-shifted *aliased sinc kernel* [37]

$$\kappa(e^{j\omega}) = e^{-j\frac{N-1}{2}\omega} \frac{\sin(N\omega/2)}{N \sin(\omega/2)}. \quad (25)$$

Since $\kappa(\omega_0) = 1$, $\kappa(\omega_k) = 0$ for $k = 1, \dots, N-1$, and other ω smoothly connects those points, $H_N(e^{j\omega})$ is an interpolation of the frequency-sampled points $(\omega_k, H(e^{j\omega_k}))$ (see Figure 2).

C. Proof of the Equation 6

Using equation (5), we can rewrite the deviation as

$$\|H - H_N\|_2^2 = \sum_{n=0}^{N-1} \left| \sum_{m=1}^{\infty} h[mN+n] \right|^2 + \sum_{n=N}^{\infty} |h[n]|^2. \quad (26)$$

With the triangle inequality and $\|X\|_2^2 \leq \|X\|_1^2$, we can upper-bound $\|H - H_N\|_2^2$ with $2S_N^2$ where $S_N = \sum_{n=N}^{\infty} |h[n]|$ is an absolute sum of the tail of the original IR $h[n]$ ($n \geq N$).

Then, we expand $h[n]$ with *partial fraction expansion* (PFE) [62], [63]. If $H(z)$ has M distinct poles where each pole ν_i has multiplicity r_i , we can express $h[n]$ as a sum of an FIR $h^{\text{FIR}}[n]$ and IIRs $h_{i,k}^{\text{PFE}}[n]$ where their transfer functions satisfy

$$H(z) = H^{\text{FIR}}(z) + \sum_{i=1}^M \sum_{k=1}^{r_i} \underbrace{\frac{\zeta_{i,k}}{(1 - \nu_i z^{-1})^k}}_{H_{i,k}^{\text{PFE}}(z)} \quad (27)$$

where $\zeta_{i,k} \in \mathbb{C}$. Applying the triangle inequality to the PFE summation gives an upper bound of S_N , an absolute sum of the tails of all PFE terms.

$$S_N \leq \sum_{i=1}^M \sum_{k=1}^{r_i} \underbrace{\sum_{n=N}^{\infty} \underbrace{|h_{i,k}^{\text{PFE}}[n]|}_{O(n^{k-1}|\nu_i|^n)}}_{O(N^{k-1}|\nu_i|^N)} = U_N. \quad (28)$$

$$\underbrace{\hspace{10em}}_{O(N^{r_i-1}|\nu_i|^N)}$$

We ignored $h^{\text{FIR}}[n]$ since N is larger than its length in practice. The PFE terms and their summations asymptotically decrease as under-braced in equation (28) [63]. We conclude the proof:

$$\|H - H_N\|_2 \leq \sqrt{2}S_N \leq \sqrt{2}U_N = \sum_{i=1}^M O(N^{r_i-1}|\nu_i|^N). \quad (29)$$

D. Proof of the Equation 7

For simplicity, we denote $H(e^{j\omega})$ and $\partial X/\partial p$ with H and X' , respectively. Since $(X_N)' = (X')_N$, we denote the composition with X'_N . Then, the squared l_2 loss gradient deviation can be written as $\Delta\mathcal{G} = |\int_0^{2\pi} H(\hat{H}' - \hat{H}'_N) + \hat{H}\hat{H}' - \hat{H}_N\hat{H}'_N d\omega/\pi|$. We upper-bound $\Delta\mathcal{G}$ with integral inequalities as

$$\Delta\mathcal{G} \leq \underbrace{\int_0^{2\pi} |H(\hat{H}' - \hat{H}'_N)| \frac{d\omega}{\pi}}_{\leq 2\|H\|_2\|\hat{H}' - \hat{H}'_N\|_2} + \underbrace{\int_0^{2\pi} |\hat{H}\hat{H}' - \hat{H}_N\hat{H}'_N| \frac{d\omega}{\pi}}_{\leq 2\|\hat{H}\hat{H}' - \hat{H}_N\hat{H}'_N\|_2} \quad (30)$$

where the under-braced ones are the Cauchy-Schwartz inequalities. Considering the first integral's upper bound, $\|H\|_2$ is a finite constant. In $\|\hat{H}' - \hat{H}'_N\|_2$, \hat{H}' is another stable LTI filter if p is well-defined. If ν_i is a function of p , its multiplicity r_i is doubled in \hat{H}' . In the worst case, p controls every pole of \hat{H} and $\|\hat{H}' - \hat{H}'_N\|_2 = \sum_{i=1}^M O(N^{2r_i-1}|\nu_i|^N)$ holds. Similarly, the upper bound of the second integral consists an l_2 distance between $\hat{H}\hat{H}'$ and $\hat{H}_N\hat{H}'_N$. Since $\hat{H}\hat{H}'$ has $2r_i$ or $3r_i$ multiplicity for each pole ν_i , $\|\hat{H}\hat{H}' - \hat{H}_N\hat{H}'_N\|_2 = \sum_{i=1}^M O(N^{3r_i-1}|\nu_i|^N)$ holds at the worst case, which concludes the proof.

Note that the SVF-parameterized differentiable IIR filter shows better asymptotic behavior than equation (7) since each SVF is independently parameterized. For $\hat{H}(z) = \prod_i \hat{H}_i^{\text{SVF}}(z)$, its derivative with respect to $p_j \in \{f_j, R_j, m_j^{\text{LP}}, m_j^{\text{BP}}, m_j^{\text{HP}}\}$ only affects \hat{H}_i^{SVF} . If $p_j \in \{f_j, R_j\}$, the gradient deviation is $\Delta\mathcal{G}^{\text{SVF}} = O(N^{3r_j-1}|\nu_j|^N) + \sum_{i \neq j} O(N^{2r_i-1}|\nu_i|^N)$. Otherwise, i.e., $p_j \in \{m_j^{\text{LP}}, m_j^{\text{BP}}, m_j^{\text{HP}}\}$ there is no pole doubling with the derivative and $\Delta\mathcal{G}^{\text{SVF}} = \sum_i O(N^{2r_i-1}|\nu_i|^N)$ holds.

REFERENCES

- [1] J. W. Bayless, "Innovations in studio design and construction in the capitol tower recording studios," *Journal of the Audio Engineering Society*, vol. 5, no. 2, pp. 71–76, April 1957.
- [2] B. A. Blesser, "An interdisciplinary synthesis of reverberation viewpoints," *Journal of the Audio Engineering Society*, vol. 49, no. 10, pp. 867–903, October 2001.
- [3] J. Traer and J. H. McDermott, "Statistics of natural reverberation enable perceptual separation of sound and space," *Proceedings of the National Academy of Sciences*, vol. 113, no. 48, pp. E7856–E7865, 2016.
- [4] V. Välimäki, J. D. Parker, L. Savioja, J. O. Smith, and J. S. Abel, "Fifty years of artificial reverberation," *IEEE Transactions on Audio, Speech, and Language Processing*, vol. 20, no. 5, pp. 1421–1448, 2012.
- [5] V. Välimäki, J. Parker, L. Savioja, J. O. Smith, and J. Abel, "More than 50 years of artificial reverberation," *Journal of the Audio Engineering Society*, January 2016.
- [6] J. Dattorro, "Effect design, part 1: reverberator and other filters," *Journal of the Audio Engineering Society*, vol. 45, no. 9, pp. 660–684, September 1997.
- [7] E. De Sena, H. Hachhabiboğlu, Z. Cvetković, and J. O. Smith, "Efficient synthesis of room acoustics via scattering delay networks," *IEEE/ACM Transactions on Audio, Speech, and Language Processing*, vol. 23, no. 9, pp. 1478–1492, 2015.
- [8] N. Agus, H. Anderson, J.-M. Chen, S. Lui, and D. Herremans, "Minimally simple binaural room modeling using a single feedback delay network," *Journal of the Audio Engineering Society*, vol. 66, no. 10, pp. 791–807, October 2018.
- [9] W. G. Gardner, "A real-time multichannel room simulator," *Journal of the Acoustical Society of America*, vol. 92, pp. 2395–2395, 1992.
- [10] A. Sarroff and R. Michaels, "Blind arbitrary reverb matching," in *Proceedings of the 23rd International Conference on Digital Audio Effects*, 2020.
- [11] V. Välimäki, B. Holm-Rasmussen, B. Alary, and H.-M. Lehtonen, "Late reverberation synthesis using filtered velvet noise," *Applied Sciences*, vol. 7, no. 5, 2017.

- [12] J.-M. Jot and A. Chaigne, "Digital delay networks for designing artificial reverberators," *Journal of the Audio Engineering Society*, February 1991.
- [13] F. Gao and W. Snelgrove, "An adaptive backpropagation cascade iir filter," *IEEE Transactions on Circuits and Systems II: Analog and Digital Signal Processing*, vol. 39, no. 9, pp. 606–610, 1992.
- [14] A. D. Back and A. C. Tsoi, "Fir and iir synapses, a new neural network architecture for time series modeling," *Neural Computation*, vol. 3, no. 3, pp. 375–385, 1991.
- [15] P. Campolucci, A. Uncini, and F. Piazza, "Fast adaptive iir-mlp neural networks for signal processing applications," in *1996 IEEE International Conference on Acoustics, Speech, and Signal Processing Conference Proceedings*, vol. 6, 1996, pp. 3529–3532 vol. 6.
- [16] J. D. P. Boris Kuznetsov and F. Esqueda, "Differentiable iir filters for machine learning application," in *Proceedings of the 23rd International Conference on Digital Audio Effects*, 2020.
- [17] L. Rabiner, B. Gold, and C. McGonegal, "An approach to the approximation problem for nonrecursive digital filters," *IEEE Transactions on Audio and Electroacoustics*, vol. 18, no. 2, pp. 83–106, 1970.
- [18] S. Nercessian, "Neural parametric equalizer matching using differentiable biquads," in *Proceedings of the 23rd International Conference on Digital Audio Effects*, 2020.
- [19] J.-M. Jot, "An analysis/synthesis approach to real-time artificial reverberation," in *[Proceedings] ICASSP-92: 1992 IEEE International Conference on Acoustics, Speech, and Signal Processing*, vol. 2, 1992, pp. 221–224 vol.2.
- [20] J. Coggin and W. Pirkle, "Automatic design of feedback delay network reverb parameters for impulse response matching," *Journal of the Audio Engineering Society*, September 2016.
- [21] J. Shen and R. Duraiswami, "Data-driven feedback delay network construction for real-time virtual room acoustics," in *Proceedings of the 15th International Conference on Audio Mostly*, ser. AM '20. New York, NY, USA: Association for Computing Machinery, 2020, p. 46–52.
- [22] N. Peters, J. Choi, and H. Lei, "Matching artificial reverb settings to unknown room recordings: a recommendation system for reverb plugins," *Journal of the Audio Engineering Society*, October 2012.
- [23] C. J. Steinmetz and J. D. Reiss, "Efficient neural networks for real-time analog audio effect modeling," *arXiv preprint arXiv:2102.06200*, 2021.
- [24] S. Billings and S. Fakhouri, "Identification of systems containing linear dynamic and static nonlinear elements," *Automatica*, vol. 18, no. 1, pp. 15–26, 1982.
- [25] J. Engel, L. H. Hantrakul, C. Gu, and A. Roberts, "Ddsp: differentiable digital signal processing," in *International Conference on Learning Representations*, 2020.
- [26] X. Serra and J. Smith, "Spectral modeling synthesis: A sound analysis/synthesis based on a deterministic plus stochastic decomposition," *Computer Music Journal*, vol. 14, pp. 12–24, 1990.
- [27] S. Nercessian, A. Sarroff, and K. J. Werner, "Lightweight and interpretable neural modeling of an audio distortion effect using hyperconditioned differentiable biquads," *arXiv preprint arXiv:2103.08709*, 2021.
- [28] S. J. Schlecht and E. A. P. Habets, "Time-varying feedback matrices in feedback delay networks and their application in artificial reverberation," *The Journal of the Acoustical Society of America*, vol. 138, no. 3, pp. 1389–1398, 2015.
- [29] V. Zavalishin, *The Art of VA Filter Design*. Native Instruments, 2020.
- [30] R. Ratnam, D. L. Jones, B. C. Wheeler, W. D. O'Brien, C. R. Lansing, and A. S. Feng, "Blind estimation of reverberation time," *The Journal of the Acoustical Society of America*, vol. 114, no. 5, pp. 2877–2892, 2003.
- [31] J. Y. C. Wen, E. A. P. Habets, and P. A. Naylor, "Blind estimation of reverberation time based on the distribution of signal decay rates," in *2008 IEEE International Conference on Acoustics, Speech and Signal Processing*, 2008, pp. 329–332.
- [32] H. Gamper and I. J. Tashev, "Blind reverberation time estimation using a convolutional neural network," in *2018 16th International Workshop on Acoustic Signal Enhancement (IWAENC)*, 2018, pp. 136–140.
- [33] S. Li, R. Schlieper, and J. Peissig, "A hybrid method for blind estimation of frequency dependent reverberation time using speech signals," in *ICASSP 2019 - 2019 IEEE International Conference on Acoustics, Speech and Signal Processing (ICASSP)*, 2019, pp. 211–215.
- [34] S. Schlecht and E. Habets, "Accurate reverberation time control in feedback delay networks," in *Proceedings of the 20th International Conference on Digital Audio Effects*, September 2017.
- [35] K. Prawda, V. Välimäki, and S. Schlecht, "Improved reverberation time control for feedback delay networks," in *Proceedings of the 22nd International Conference on Digital Audio Effects*, September 2019.
- [36] E. T. Chourdakis and J. D. Reiss, "A machine-learning approach to application of intelligent artificial reverberation," *Journal of the Audio Engineering Society*, vol. 65, no. 1/2, pp. 56–65, January 2017.
- [37] J. O. Smith, *Spectral Audio Signal Processing*. W3K Publishing, 2011.
- [38] A. Wishnick, "Time-varying filters for musical applications," in *Proceedings of the 17th International Conference on Digital Audio Effects*, 2014.
- [39] V. Välimäki, H.-M. Lehtonen, and M. Takanen, "A perceptual study on velvet noise and its variants at different pulse densities," *IEEE Transactions on Audio, Speech, and Language Processing*, vol. 21, no. 7, pp. 1481–1488, 2013.
- [40] H. Järveläinen and M. Karjalainen, "Reverberation modeling using velvet noise," *Journal of the audio engineering society*, March 2007.
- [41] M. R. Schroeder and B. F. Logan, "'colorless' artificial reverberation," *Journal of the Audio Engineering Society*, vol. 9, no. 3, pp. 192–197, July 1961.
- [42] Y. Bengio, N. Léonard, and A. C. Courville, "Estimating or propagating gradients through stochastic neurons for conditional computation," *arXiv preprint arXiv:1308.3432*, 2013.
- [43] S. Schlecht, "Fdntb: The feedback delay network toolbox," in *Proceedings of the 23rd International Conference on Digital Audio Effects*, October 2020.
- [44] D. Rocchesso and J. O. Smith, "Circulant and elliptic feedback delay networks for artificial reverberation," *IEEE Transactions on Speech and Audio Processing*, vol. 5, no. 1, pp. 51–63, 1997.
- [45] R. Väänänen, V. Välimäki, J. Huopaniemi, and M. Karjalainen, "Efficient and parametric reverberator for room acoustics modeling," 09 1997.
- [46] J. Chung, C. Gulcehre, K. Cho, and Y. Bengio, "Empirical evaluation of gated recurrent neural networks on sequence modeling," *arXiv preprint arXiv:1412.3555*, 2014.
- [47] J. L. Ba, J. R. Kiros, and G. E. Hinton, "Layer normalization," *arXiv preprint arXiv:1607.06450*, 2016.
- [48] P. Svensson and U. R. Kristiansen, "Computational modelling and simulation of acoustic spaces," *Journal of the Audio Engineering Society*, June 2002.
- [49] R. Scheibler, E. Bezzam, and I. Dokmanic, "Pyroomacoustics: A python package for audio room simulations and array processing algorithms," *arXiv preprint arXiv:1710.04196*, 2017.
- [50] S. Shelley and D. Murphy, "Openair: An interactive auralization web resource and database," *129th Audio Engineering Society Convention 2010*, vol. 2, pp. 1270–1278, 01 2010.
- [51] J. Eaton, N. D. Gaubitch, A. H. Moore, and P. A. Naylor, "Estimation of room acoustic parameters: The ace challenge," *IEEE/ACM Transactions on Audio, Speech, and Language Processing*, vol. 24, no. 10, pp. 1681–1693, 2016.
- [52] G. Defrance, L. Daudet, and J.-D. Polack, "Finding the onset of a room impulse response: straightforward?" *The Journal of the Acoustical Society of America*, vol. 124, no. 4, pp. EL248–EL254, 2008.
- [53] J. Yamagishi, C. Veaux, K. MacDonald *et al.*, "Cstr vctk corpus: English multi-speaker corpus for cstr voice cloning toolkit (version 0.92)," 2019.
- [54] D. P. Kingma and J. Ba, "Adam: A method for stochastic optimization," *arXiv preprint arXiv:1412.6980*, 2017.
- [55] "Acoustics — Measurement of room acoustic parameters — Part 2: Reverberation time in ordinary rooms," International Organization for Standardization, Geneva, CH, Standard, Mar. 2008.
- [56] C. Hak, R. Wenmaekers, and L. Luxemburg, "Measuring room impulse responses: Impact of the decay range on derived room acoustic parameters," *Acta Acustica united with Acustica*, vol. 98, 11 2012.
- [57] Z. Meng, F. Zhao, and M. He, "The just noticeable difference of noise length and reverberation perception," in *2006 International Symposium on Communications and Information Technologies*, 2006, pp. 418–421.
- [58] M. G. Blevins, A. Buck, Z. E. Peng, and L. Wang, "Quantifying the just noticeable difference of reverberation time with band-limited noise centered around 1000 hz using a transformed up-down adaptive method," June 2013.
- [59] J. Bradley, R. Reich, and S. Norcross, "A just noticeable difference in c50 for speech," *Applied Acoustics*, vol. 58, no. 2, pp. 99 – 108, 1999.
- [60] F. Martellotta, "The just noticeable difference of center time and clarity index in large reverberant spaces," *The Journal of the Acoustical Society of America*, vol. 128, pp. 654–63, 08 2010.
- [61] E. Larsen, N. Iyer, C. Lansing, and A. Feng, "On the minimum audible difference in direct-to-reverberant energy ratio," *The Journal of the Acoustical Society of America*, vol. 124, pp. 450–61, 07 2008.
- [62] J. Liski, B. Bank, J. Smith, and V. Välimäki, "Converting series biquad filters into delayed parallel form: Application to graphic equalizers," *IEEE Transactions on Signal Processing*, vol. PP, pp. 1–1, 05 2019.
- [63] J. O. Smith, *Introduction to Digital Filters with Audio Applications*. W3K Publishing, 2007.